High-Resolution Modeling of Typhoon Morakot (2009): Vortex Rossby Waves and Their Role in Extreme Precipitation over Taiwan

JONATHAN D. HALL AND MING XUE

Center for Analysis and Prediction of Storms, and School of Meteorology, University of Oklahoma, Norman, Oklahoma

LINGKUN RAN

Center for Analysis and Prediction of Storms, University of Oklahoma, Norman, Oklahoma, and Institute of Atmospheric Physics, Chinese Academy of Sciences, Beijing, China

LANCE M. LESLIE

School of Meteorology, University of Oklahoma, Norman, Oklahoma

(Manuscript received 21 December 2011, in final form 27 July 2012)

ABSTRACT

A high-resolution nonhydrostatic numerical model, the Advanced Regional Prediction System (ARPS), was used to simulate Typhoon Morakot (2009) as it made landfall over Taiwan, producing record rainfall totals. In particular, the mesoscale structure of the typhoon was investigated, emphasizing its associated deep convection, the development of inner rainbands near the center, and the resultant intense rainfall over western Taiwan.

Simulations at 15- and 3-km grid spacing revealed that, following the decay of the initial inner eyewall, a new, much larger eyewall developed as the typhoon made landfall over Taiwan. Relatively large-amplitude wave structures developed in the outer eyewall and are identified as vortex Rossby waves (VRWs), based on the wave characteristics and their similarity to VRWs identified in previous studies.

Moderate to strong vertical shear over the typhoon system produced a persistent wavenumber-1 (WN1) asymmetric structure during the landfall period, with upward motion and deep convection in the downshear and downshear-left sides, consistent with earlier studies. This strong asymmetry masks the effects of WN1 VRWs. WN2 and WN3 VRWs apparently are associated with the development of deep convective bands in Morakot's southwestern quadrant. This occurs as the waves move cyclonically into the downshear side of the cyclone. Although the typhoon track and topographic enhancement contribute most to the record-breaking rainfall totals, the location of the convective bands, and their interaction with the mountainous terrain of Taiwan, also affect the rainfall distribution. Quantitatively, the 3-km ARPS rainfall forecasts are superior to those obtained from coarser-resolution models.

1. Introduction

Tropical cyclones (TCs) often produce widespread destruction and loss of life. They can generate severe weather, including destructive winds, storm surge flooding, and tornadoes, for extended periods over relatively large spatial areas. Another TC threat that has arguably received less attention is extreme rainfall, leading to severe freshwater flooding and, in geologically susceptible areas, landslides causing loss of life and property damage. Improvements in quantitative precipitation forecasting (QPF) with TCs, especially at the extreme end of the rainfall spectrum, and with 1–2-day lead times, could reduce the loss of life through, for example, evacuation of vulnerable communities.

A recent case where improved QPF would have been very beneficial is Typhoon Morakot in August 2009, which claimed a heavy toll in lives lost and infrastructure damage over the northwestern Pacific. The impact on Taiwan was devastating, with about 700 lives lost and NT$110 billion (New Taiwan dollars; $3.3 billion U.S.

dollars) in damage, mainly owing to freshwater flooding and debris flows. This devastation was almost entirely due to the extreme rainfall Morakot produced over southern Taiwan, including 1404 mm in 24 h at Weiliao Mountain in Pingtung County, and a 3-day storm total of 2884 mm at Alishan (Wu and Yang 2011). Both are records for Taiwan and close to world records.

Taiwan is regularly affected by tropical cyclone impacts; for example, Zhang et al. (2009) indicate that about 1.8 TCs per year made landfall on the island over the period 1983–2006. Furthermore, the island's steep topography featuring a spine of roughly north–south-orientated mountains reaching above 3000-m altitude, frequently generates complex effects on both the rainfall distribution through micro- and mesoscale topographic enhancement, and the structure and track of the TC itself, as the inner convective bands of the TC interact with the topography. Taiwan's location near the climatological position of the monsoon trough during the main typhoon season can also significantly affect the rainfall distribution through interactions with the typhoon's circulation. There are many case studies of Taiwan TC events, in particular of the distribution of total rainfall accumulation for each event, and the effects on the TC track during its passage nearby, or over, the island. For example, Lin et al. (2002) investigated the rainfall distribution produced by Super Typhoon Bilis (2000), in particular the orographic influence of up-slope flow on the eastern flanks of Taiwan's Central Mountain Range (CMR). They compared the observed rainfall distribution with that calculated using a flux model of orographic rainfall forced by the simulated wind and moisture field of the typhoon, using 15- and 5-km-resolution versions of the Coupled Ocean–Atmosphere Mesoscale Prediction System (COAMPS). They concluded that orographic forcing, rather than the original rainbands of the typhoon, controlled heavy rainfall in the vicinity of the mountains. Chiao and Lin (2003) used a similar methodology for Tropical Storm Rachel and found evidence that topographic enhancement of preexisting convective bands, along with more local topographically induced flows and deep convection, were important factors in the observed rainfall distribution. Wu et al. (2002) investigated the impact of Typhoon Herb (1996), and also found strong topographic forcing was critical to accumulated rainfall during the event, especially at the heavy rainfall end of the distribution. Yang et al. (2008) studied the structural changes and rainfall distribution produced by Typhoon Nari (2001) as it made landfall over Taiwan. They found that both wavenumber-1 (WN1) asymmetries in the flow associated with the environmental vertical shear, along with topographic enhancement could in large part account for the distribution of heavy rainfall

during the event. The interaction of a typhoon with northeasterly monsoon in the vicinity of Taiwan and topography was investigated by Wu et al. (2009b), who found that the spatial distribution of the heavy rainfall was sensitive to topographic forcing and changes in the simulated vortex, both of which affected the interaction with the northeast monsoon flow. In a similar fashion, Chien et al. (2008) and Lee et al. (2008) studied the rainfall distribution over Taiwan associated with the interaction between Typhoon Mindulle (2004) and the southwest monsoon. They found that a secondary low, which formed off the western coast of Taiwan as the typhoon made landfall over the northeast of the island, played an important role in the development of deep convective banding in the convergent flow between the secondary low and the southwesterly monsoon off the western coast of Taiwan. These convective bands led to enhanced rainfall where they impinged on the western slopes of the CMR. In some aspects, this was a similar evolution to that of Morakot. Despite the relatively high frequency with which Taiwan is affected by TC impacts, the rainfall accumulations observed during Typhoon Morakot's passage over the island were records for Taiwan and were close to world records.

QPF attempts to forecast intensity and duration of rainfall at particular geographical locations. At the high intensity part of the rainfall spectrum, QPF is challenging, mainly because high rainfall rates are associated with deep convection and, more specifically, its initiation and organization on meso- and convective scales. Observational studies have shown that the strong TC circulation dynamically organizes deep convection and associated intense rainfall near the TC core (e.g., Burpee and Black 1989; Marks 1985), leading to a strong dependence of rainfall on the TC track. Further confirmation was provided by the QPF study of Tuleya et al. (2007). Lonfat et al. (2004) used Tropical Rainfall Measuring Mission (TRMM) satellite data to highlight the asymmetrical distribution of rainfall in TCs. They showed that in the near core area, azimuthal asymmetries contribute up to 50% of the azimuthal-mean rainfall rate, although this proportion decreases as the TC intensity increases, leading to large variations in rainfall intensities and accumulated rainfall totals. Interaction with land surface and topography is also an important, complex factor as it depends on storm intensity and size, and the track geometry relative to the topography (Smith and Barstad 2004). Furthermore, the interaction of a TC with synoptic-scale features in its environment, such as baroclinic midlatitude or monsoon troughs, can produce rainfall asymmetries that affect accumulations (e.g., Atallah and Bosart 2003). In summary, accurate QPF for a landfalling TC requires accurate track forecasts, and realistic

treatment of mesoscale processes in the eyewall and inner core of the cyclone, accurate depictions of topographic forcing, interactions of the TC with its environment, and nonlinear interactions between these processes. All are important for Morakot.

The dynamical and explicit approach to QPF utilizing high-resolution numerical models is in its infancy. Most studies involving high-resolution (horizontal grid spacing less than 10 km) modeling of TCs have been mainly concerned with the mesoscale structure of the cloud and wind fields, and less so on the QPF problem. More recent studies including Zhao and Xue (2009), Dong and Xue (2012), Li et al. (2012), and Du et al. (2012) specifically addressed the QPF problem of a landfalling hurricane, through assimilation of high-resolution coastal or airborne Doppler radar data using different assimilation methods. Zhao et al. (2012), by assimilating data from radars over the Taiwan island and coastal regions of mainland China, obtained skillful precipitation forecasts for a landfalling typhoon interacting with coastal mountains in southeastern China.

Typhoon Morakot, not surprisingly, has prompted much interest in numerically replicating the observed rainfall amount and pattern. To date, most work has been focusing on the influence of Morakot track prediction, and the interaction of Morakot's circulations with the broader monsoon flow and with the Taiwan orography. A short paper by Ge et al. (2010) simulated Morakot using the Advanced Research Weather Research and Forecasting model (ARW-WRF) with 3-km grid spacing and suggested that the excessive rainfall was due mainly to persistent convergence between a very moist southwesterly monsoon flow and the northerly flow on the western flank of Morakot, and the high topography of Taiwan. Lin et al. (2010) used the ARW-WRF at a coarser 10-km grid spacing, with similar findings, but claimed that they produced a better representation of the most intense rainfall area (storm total accumulations higher than 2000 mm). Wu et al. (2011) and Liang et al. (2011) emphasized the role of the multiscale monsoonal flows in the supply of moist air. They found that the slowing of Morakot's track and its northward deflection during the Taiwan landfall stage is closely related to low-frequency variations in the monsoon flow, leading to southern Taiwan's long exposure to enhanced convection on the southern side of the typhoon. Nguyen and Chen (2011) primarily focused on vortex initialization using WRF at 6-km grid spacing, but also found that the model run with the highest quality track forecast produced a skillful rainfall forecast over southern Taiwan. Hendricks et al. (2011) used the Naval Research Laboratory's Coupled Ocean/Atmosphere Mesoscale Prediction System for Tropical Cyclones (COAMPS-TC) in a triply nested configuration, with a 5-km inner, system-following mesh to simulate the landfall phase of Morakot. They too found the model was able to reproduce the track, broad structure of the convective organization and intensity of the typhoon, leading to a qualitatively reasonable spatial pattern of rainfall accumulation over Taiwan. However, the model generally underpredicted total rainfall, and this was attributed in part to errors in the track forecast and inaccuracies in the location and timing of mesoscale convective elements and stratiform precipitation. Huang et al. (2011) utilized a similar grid configuration using the fifth generation Pennsylvania State University–National Center for Atmospheric Research Mesoscale Model (MM5) to show the importance of the environmental southwesterly monsoon flow and its enhancement by Tropical Storm Goni to the southwest.

Other studies have adopted an ensemble approach to define sensitivities and uncertainties in the dynamical evolution of Morakot's interaction with the environment and the resultant rainfall. Zhang et al. (2010) used the ARW-WRF at 4.5-km grid spacing with 62 ensemble members. Perturbed initial conditions were provided by a global ensemble Kalman filter (EnKF) data assimilation system (Whitaker et al. 2008). The majority of members, including the control members, qualitatively reproduced the heavy rainfall reasonably well. However, there was considerable variation in the typhoon's track and intensity, which they ascribed to topographic interaction, leading to a large spread of total rainfall. A similar ensemble study by Fang et al. (2011), utilizing ARW-WRF at 4-km grid spacing, found considerable topographic forcing of both the track and rainfall patterns.

Although it is well known that mesoscale asymmetries near the TC core can strongly influence the resultant rainfall accumulation, as outlined above, none of the previously published studies on Typhoon Morakot just described focused on the mesoscale asymmetric structures in Morakot, and the importance of their roles in producing the extreme rainfall. In recent times, much of the azimuthal asymmetry near the TC core, manifest in the form of so-called secondary convective bands, has been associated with vortex Rossby wave (VRW) activity. The idea that Rossby-type waves propagating on the radial gradient of vorticity in a TC could be related to secondary convective bands was initially provided by MacDonald (1968). In the case of VRWs, the restoring force is provided by the radial gradient of vorticity, in analogy to planetary Rossby waves, where the gradient of earth's vorticity provides this restoring force. Since then, theoretical (Montgomery and Kallenbach 1997; Möller and Montgomery 2000), high-resolution modeling (Chen and Yau 2001; Wang 2002a,b; Chen et al. 2003) and observational studies (Reasor et al. 2000;

Corbosiero et al. 2006) have confirmed this link. In fact, Chen et al. (2003) used empirical normal mode analysis to show that VRW activity could account for 70%–80% of the wave activity associated with larger-scale asymmetries, and it is also interesting to note that the analysis of Corbosiero et al. (2006) was based primarily upon radar reflectivity data, rather than Doppler velocity, which would only be possible given a close relationship between asymmetric flow associated with VRWs and the rainbands. The close relationship between VRWs and asymmetric deep convection (or secondary convective bands) near the TC core suggests that VRWs may play an important role in azimuthal asymmetries in rainfall rate associated with a TC, and consequently on total rainfall accumulations.

Our high-resolution modeling and diagnostic study presented here emphasizes the impact of mesoscale structures and asymmetries of Typhoon Morakot, in particular VRWs, and their interaction with the environment on rainfall distribution. The primary aims are as follows: 1) to simulate with sufficient fidelity the track and the mesoscale structure of Morakot, particularly organized deep convection near the radius of maximum azimuthal mean wind during and shortly after the landfall stages; and 2) to explore relationships between mesoscale evolution and rainfall distribution over Taiwan. The Advanced Regional Prediction System (ARPS) is used at 15- and 3-km grid spacing, starting at several different initial times before the landfall over Taiwan. Emphasis will be placed on the 3-km results.

The rest of this paper is organized as follows: section 2 describes the numerical model ARPS and the simulation experiments; section 3 analyzes the evolution of simulated Morakot during Taiwan landfall, emphasizing mesoscale structure and VRWs; section 4 details the effect of mesoscale structure on rainfall forecasts, and quantitatively assesses the forecasts; and section 5 provides a summary and conclusions.

2. Prediction model and design of numerical experiments

The numerical model used in the simulations was version 5.2 of the Advanced Regional Prediction System (ARPS) developed at the Center for Analysis and Prediction of Storms, University of Oklahoma. Model details can be found in Xue et al. (2000, 2001, 2003). ARPS is a cloud-resolving, nonhydrostatic mesoscale model with a generalized terrain-following vertical coordinate. It was run on stationary grids with two horizontal resolutions; a coarse resolution on a large domain on a 15-km horizontal grid, and high-resolution runs on a 3-km grid. The 15-km domain covered an area of 9045 km × 6045 km
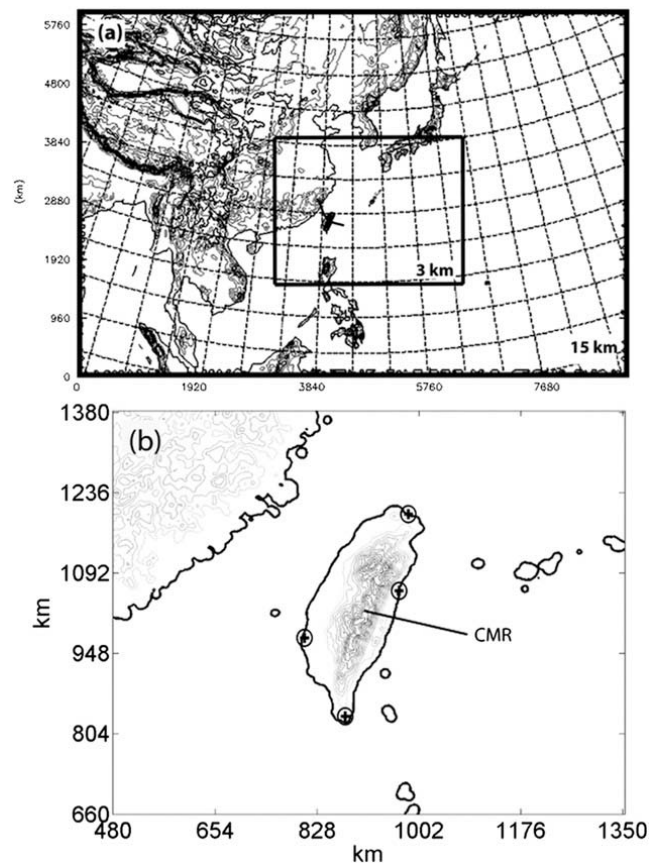

FIG. 1. Geographical domain and grid setup for ARPS model simulations, with topography used in the 3-km-resolution runs. (a) The track of Morakot is indicated and (b) the locations of peak rainfall (Alishan), and four observational CWB radar sites are shown. Origin of axes in (b) is the southwestern corner of the 3-km grid.

centered at 28°N, 125°E, while the 3-km grid spanned 3009 km × 2409 km, covering Taiwan. For a depiction of the grids, see Fig. 1. The model had 53 stretched vertical levels and the model top was at a height of 20 km. The vertical grid spacing was about 50 m near the surface, 750 m at the model top, and had an overall average of 400 m. The hyper-tangent function stretching option as described in Xue et al. (1995) was used with a tuning parameter value of 0.2. Physics packages used included a 1.5-order closure subgrid-scale turbulence scheme with a nonlocal treatment of the planetary boundary layer. The 3-km runs were cloud resolving and treated convection explicitly using the Lin three-class ice microphysics scheme, whereas the 15-km runs also incorporated the Kain–Fritsch convective parameterization. All experiments (except one with Taiwan terrain set to zero) incorporated realistic terrain. Sea surface temperatures were from the operational National Centers for Environmental Prediction (NCEP) Global Forecast System (GFS) 0.5° global analysis and

TABLE 1. Summary of numerical simulations, where ddhh is the day and hour in UTC, in August 2009.

Experiment name	Horizontal resolution (km)	Taiwan terrain	Simulation period	Initial and boundary conditions
GFS	~54	Smoothed 30 arc sec	0700–0900	Operational real-time global model forecast
A15_ddhh	15	Smoothed 30 arc sec	ddhh–0900	Initial and boundary conditions from GFS analyses and 3-h forecasts
A3_ddhhT	3	30 arc sec (~9 km)	ddhh–0900	Initial and boundary conditions from GFS analyses and 3-h forecasts
A3_ddhhNT	3	None	ddhh–0900	Identical to A3_ddhhT, except Taiwan topography is flattened

held fixed during the integration. A two-layer land surface model was included with surface characteristics defined by high-resolution land-use/land cover datasets, and initialized using the GFS soil model states in its analysis. The Goddard Space Flight Center long and shortwave radiation package was also included. For more details and related references, please refer to Xue et al. (2000, 2001).

A major difficulty associated with high-resolution modeling of TCs is obtaining an initial vortex to accurately represent the system during the integration. For Morakot, its very large size was helpful, as the operational GFS analyses on the 0.5° grid were of acceptable quality, after a short period of spinup, for initializing the ARPS runs and for lateral boundary conditions. This procedure was used for both 15- and 3-km runs, with lateral boundary conditions from the 6-hourly GFS analyses, interspersed with 3-h forecasts. In this study, the experiments were individual 15-km-resolution runs initialized every 6 h from 1200 UTC 5 August until 0000 UTC 8 August inclusive, and 3-km-resolution runs initialized at 3-hourly intervals between 0000 UTC 7 August and 0600 UTC 8 August inclusive. At 0300, 0900, 1500, and 2100 UTC, the 3-h GFS forecasts were used as initial conditions while at other times they were the GFS analyses. Details of model runs and the labeling scheme are given in Table 1. To better assess the effects of Taiwan terrain on the mesoscale structure of the TC, all 3-km runs with full terrain were repeated with Taiwan's terrain elevation set to zero, while retaining the same land-use characteristics as in the nonzero terrain runs. Our focus is on mesoscale structures, representing low wavenumber azimuthal departures from axisymmetry, near the radius of maximum winds of Morakot. Determining the TC center is critical for the spectrum analysis, as an inaccurate location will generate spurious asymmetries, particularly at azimuthal WN1 (Reasor et al. 2000). For Morakot's landfall phase, the complex TC structure with its distorted eyewall, and interaction with the terrain of Taiwan led to difficulties with previously used center-determination methods.

Occasionally, the circulation associated with wave motions near the eyewall was dominant enough to resemble transient centers of the TC, and circulation-based center-finding methods jumped between the "true" center and these transients. An alternative method developed here locates the TC as the geometric center of a best-fit ellipse to the ring of cyclonic vorticity associated with the outer eyewall. The ellipse was fitted to grid points in the eyewall with vorticity above a threshold, using a geometric least squares method (Gander et al. 1994). Given the Cartesian equation for the ellipse

$$by^2 + cxy + dx + ey + f = -x^2, \tag{1}$$

and a set of n points satisfying the vorticity criteria, the problem amounts to finding the set of coefficients b–f that best satisfy

$$\begin{pmatrix} y_1^2 & x_1y_1 & x_1 & y_1 & 1 \\ y_2^2 & x_2y_2 & x_2 & y_2 & 1 \\ \vdots & \vdots & \vdots & \vdots & \vdots \\ y_n^2 & x_ny_n & x_n & y_n & 1 \end{pmatrix} \begin{pmatrix} b \\ c \\ d \\ e \\ f \end{pmatrix} = \begin{pmatrix} -x_1^2 \\ -x_2^2 \\ \vdots \\ -x_n^2 \end{pmatrix}, \tag{2}$$

where (x_i, y_i) are the Cartesian coordinates of the ith point. Equation (2) is in the form $\mathbf{Mp} = \mathbf{r}$, and the minimum residual least squares solution can be found by solving $\mathbf{p} = \mathbf{M}^+\mathbf{r}$ where $\mathbf{M}^+$ is the pseudoinverse of $\mathbf{M}$. The matrix $\mathbf{M}^+$ was calculated numerically using a singular value decomposition. Through empirical trials, the threshold was chosen as 0.5 times the maximum vorticity at any grid point, which typically sampled several thousand grid points and included most of the eyewall.

An example, when Morakot was located over Taiwan, is shown in Fig. 2, and in Fig. 2d it can be seen that the procedure locates the center of the distorted annulus of cyclonic vorticity, rather than the transient center associated with a strong wave on the western side of the cyclone. The procedure was stable for the period of this study, although on rare occasions some subjective correction was needed.
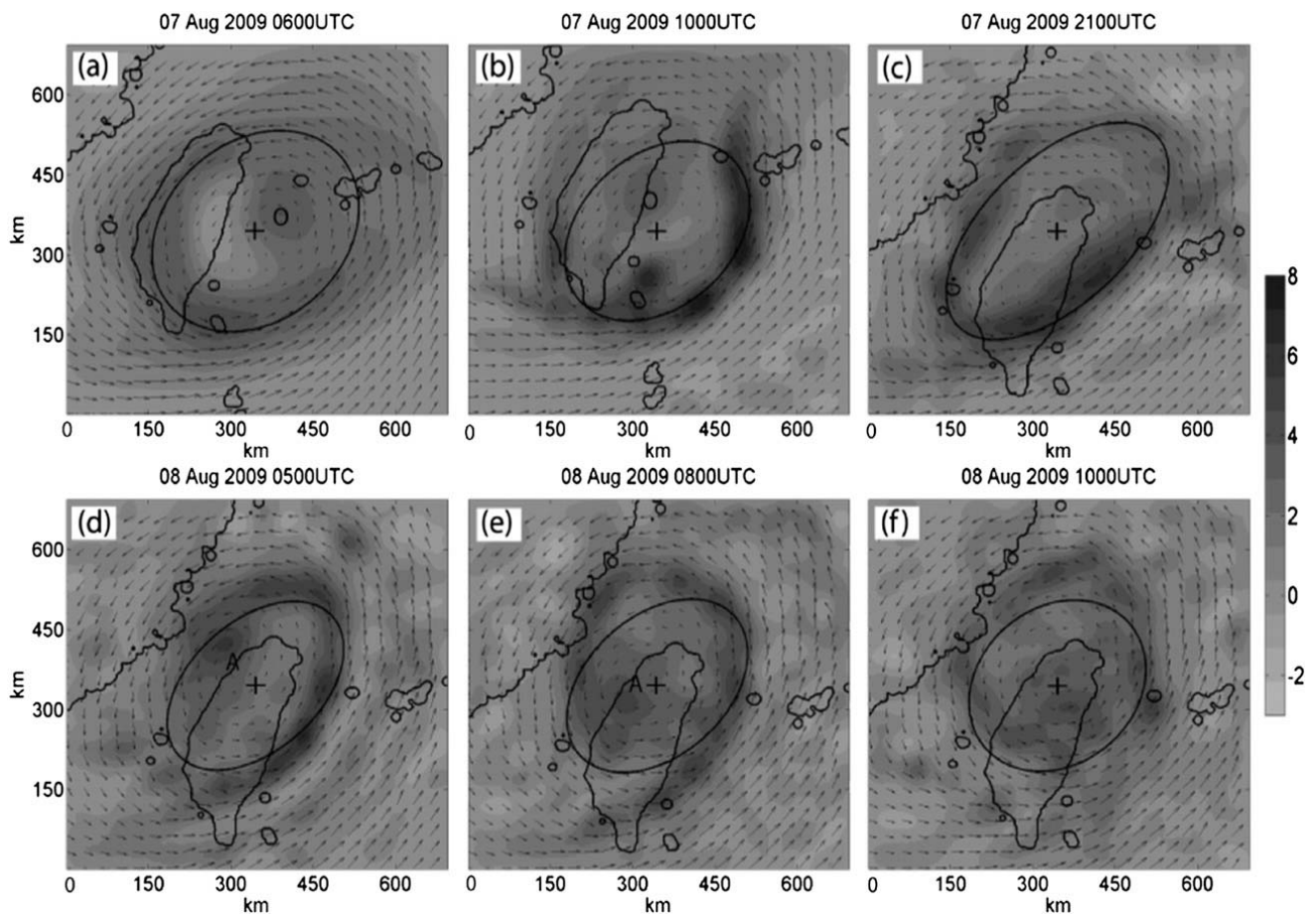
FIG. 2. Vertical component of relative vorticity at approximately 850 hPa for the A3_0700NT model run. Plus symbol indicates the center-found location based on the best-fit ellipse shown. The annotation O in (a),(b) indicates the model representation of the inner eyewall of Morakot, while A in (d),(e) indicates the center location based on pressure and wind fields, in this case associated with a transient center in the outer eyewall—this is discussed further in the text. Fields have been smoothed with a linear filter to emphasize meso- and larger scale flows.

3. Typhoon structure during landfall phase

a. Broad overview, track, and intensity predictions

Chien and Kuo (2011) provided an observational, synoptic overview of Morakot, and its relation to the rainfall event in Taiwan. Morakot developed about 1300 km east of Taiwan in early August 2009, and followed a steady, almost due west, track toward Taiwan. As shown by Chien and Kuo (2011), the large size of Morakot's circulation, combined with its slow forward speed, and extremely moist air mass over Taiwan were important synoptic-scale factors in the resultant extreme rainfall. However, as they suggested, the placement and timing of the intense rainfall was likely to be controlled by mesoscale organization of deep convection near Marakot's core.

The tracks from a selection of the ARPS simulations are shown in Fig. 3, along with the best track produced by the Central Weather Bureau, Taiwan (CWB) and

track errors of these runs are shown in Table 2. The ARPS 3-km runs consistently reproduced Morakot's track up to landfall and during its initial passage over Taiwan, both in direction and speed. However, there were discrepancies relevant to the quality of the total precipitation forecast. There was a tendency in the lower-resolution (15-km grid spacing) model runs for the TC to be deflected northward as they approached Taiwan. Typical is the A15_0700 run (Fig. 3a), where the initially westward-moving cyclone was deflected sharply to the north at about 1200 UTC 7 August, while centered about 100 km east of landfall. This motion took the TC on a track with a strong northward bias, with the 24-h track error reaching almost 100 km, which meant the center did not cross Taiwan. The GFS forecast from 0000 UTC 7 August also exhibited this tendency in the early stages (not shown). In contrast, the track of the 3-km run with the same start time (A3_0700T) was virtually identical to the CWB best track for the first
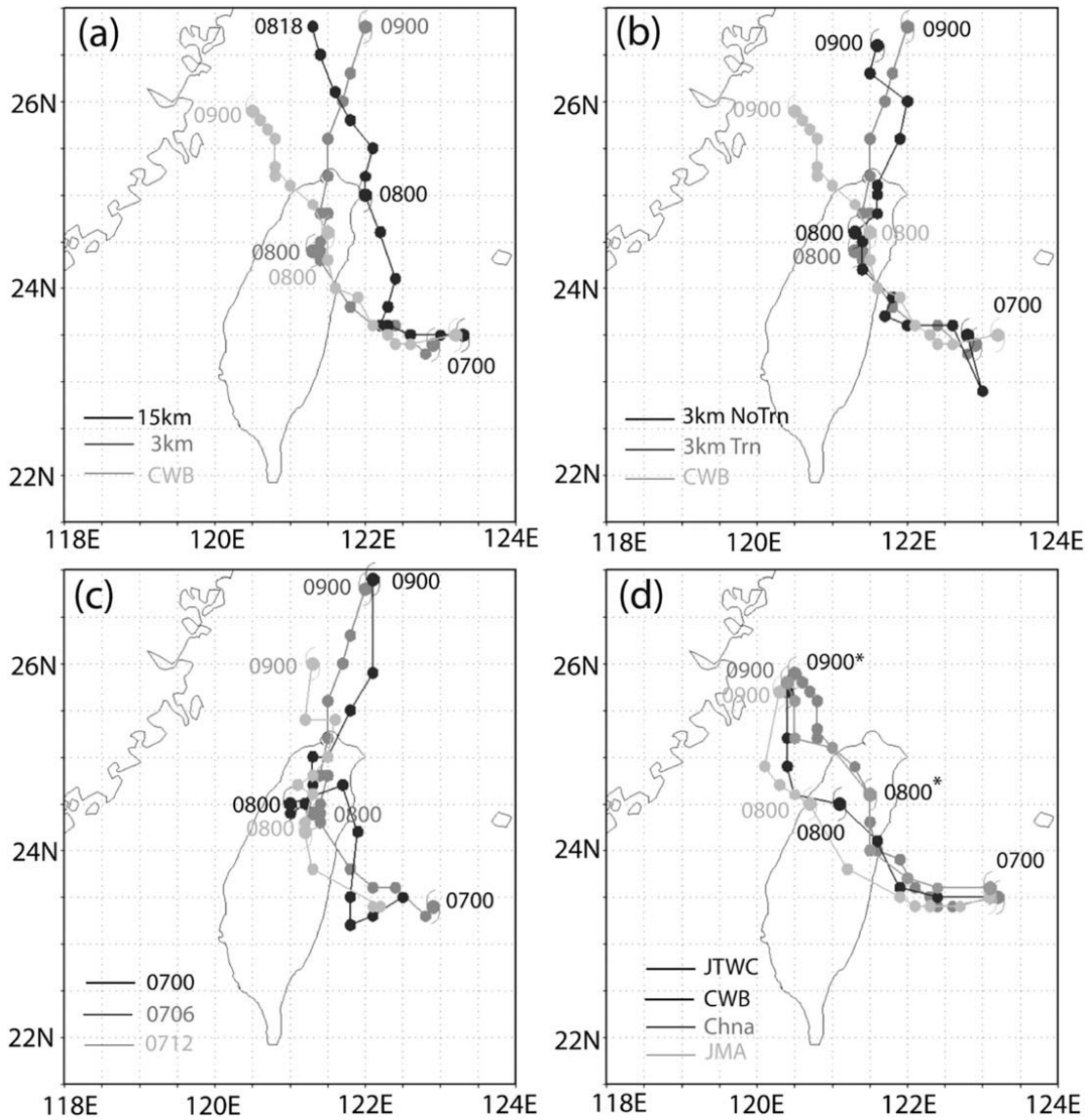
FIG. 3. Tracks of model runs for Typhoon Morakot, along with the best track from CWB: (a) A15_0700 and A3_0700T, (b) A3_0700T and A3_0700N, (c) A3_0700T, A3_0706T, and A3_0712T, and (d) best tracks from CWB, Japanese Meteorological Agency (JMA), and Joint Typhoon Warning Center (JTWC). Typhoon center locations are plotted 3 hourly with typhoon symbols at 0000 UTC 7, 8, and 9 Aug. Final positions on all tracks are at 0000 UTC 9 Aug.

day, as shown by the 24-h track error of only 29 km in Table 2. Subsequently, it developed a right-of-track (northeasterly) bias, taking the typhoon too quickly to the north and clear of Taiwan. This was characteristic of all 3-km runs, as indicated in Fig. 3b, although generally less pronounced the later the start time.

The error in the final position at 0000 UTC 9 August for A3_0712T is about half that of A3_0700T (the 0703 and 0709 tracks are omitted for visual clarity but were similar to other 3-km runs). This bias was responsible for reducing the influence time of the southern flank of the typhoon over Taiwan, and in turn it affected the predicted storm total rainfall accumulations, described

in section 4. Also evident, as indicated in Fig. 3c for the 0700 runs, is that there was little track difference between 3-km runs with and without Taiwan terrain, confirmed in corresponding later runs, suggesting only a minor vortex-scale influence of topography on the structure and track of the cyclone. Synoptically, the primary difference between the 3-km runs was the weakening of the midlevel subtropical ridge to the north of Morakot; in earlier runs, this feature weakened more rapidly (not shown), which prematurely removed its steering influence over the typhoon, and allowed the larger northeastward track bias to develop. It is therefore more likely that synoptic scale influences associated with the

TABLE 2. Forecast-track errors (km) for various model simulations, verified against the CWB best track. Tracks correspond to those plotted in Fig. 3. Year for first column is 2009.

Time and date	A3_0700T	A3_0706T	A3_0712T	A3_0700NT	A15_0700T
0000 UTC 7 Aug	32	—	—	32	20
0600 UTC 7 Aug	22	15	—	27	29
1200 UTC 7 Aug	37	52	22	34	23
1800 UTC 7 Aug	38	37	37	21	79
0000 UTC 8 Aug	29	50	52	22	98
0600 UTC 8 Aug	59	68	61	35	72
1200 UTC 8 Aug	68	53	65	78	138
1800 UTC 8 Aug	123	109	93	145	121
0000 UTC 9 Aug	175	189	78	160	128

environment of the typhoon, and errors in the simulation, were principally responsible for the track bias in the 3-km runs rather than vortex-scale influences of the Taiwan topography.

The above is broadly consistent with observations and modeling of previous typhoon impacts over Taiwan (Lin et al. 2005). Lower-resolution simulations generally maintained cyclonic vorticity and significant flow associated with the initial smaller eyewall, and they tended to be deflected on approach to landfall. The inner vorticity feature was weak in the 3-km runs, with weak flow inside the large outer radius of maximum winds. According to the scale analysis of Lin et al. (2005), there should be a weaker influence on the track in the 3-km runs, with the wind field being large relative to Taiwan terrain. The lack of influence of the topography on the Morakot's track found here is different from that in Fang et al. (2011), who found significant topographic forcing on the tracks in their 4-km-resolution model runs. The reasons are unclear, but procedural differences in objectively locating the center location may play a role. Similarly, the complexities of Morakot's structure during landfall over Taiwan, and producing the official best track presented greater than usual difficulties, reflected in the relatively large variation in subjective best tracks produced by various agencies (Fig. 3d). With differences in these best tracks reaching 80 km during Morakot's passage over Taiwan (which is larger than most 24-h track errors shown in Table 2), caution is necessary in comparing model tracks to any particular "ground truth". Henceforth, the CWB best track will be used as the reference, but with this caveat in mind.

Morakot peaked in intensity with estimated sustained winds of 40 m s^{-1} while still well off the eastern coast of Taiwan, associated with an eyewall with a radius of about 55 km. As the cyclone approached the coast, it experienced moderate to strong north-northeasterly vertical wind shear. Infrared satellite imagery seen in Fig. 4, and radar imagery from Taiwan CWB radars in Fig. 5, showed that the deep convection was asymmetric during this period, and became increasingly confined to the southern semicircle of the cyclone as landfall was approached and the initial eyewall weakened (Fig. 4a, and Figs. 5a,b). Cold convective cloud tops were almost absent for several hours while the TC was centered over Taiwan (Fig. 4b). Redevelopment of vigorous deep convection near western Taiwan evident in Fig. 4c and Fig. 4d and in later radar imagery (Fig. 5) is important and is discussed below.

Intensity time series of maximum wind speed for the A3_0700T and A15_0700 runs are shown in Fig. 6. The initial vortex was too weak, as the initial smaller, decaying eyewall was not resolved well in the GFS analysis. However, wind speeds in the outer eyewall increased rapidly in the first 3 h in the 3-km run, and less rapidly but steadily for 12–14 h in the 15-km run. The spunup maximum wind speeds closely matched the estimated maxima for the best tracks as the outer wind maximum became dominant. There was a further gradual increase in intensity in the 3-km simulation even after the center made landfall over Taiwan. However, there was little difference between the maximum winds between the 3- and 15-km runs between hours 12 and 30, despite the center of the 3-km run making landfall, while the 15-km run did not (Fig. 3a). This is likely due to the large size of Morakot relative to Taiwan, so much of the outer eyewall was over the ocean, despite the center being over land. The best tracks showed a weakening trend following landfall over Taiwan, resulting in a large bias in the simulations. However, the cautionary note regarding the best track is more pertinent for intensity, where a strong reliance on the Dvorak method of intensity estimation (Dvorak 1984), in the absence of other observations, is problematic for such a complex TC.

b. Mesoscale structure and vortex Rossby waves

Morakot exhibited considerable mesoscale structure in its broad outer eyewall during its landfall phase over Taiwan. Radar data from Taiwan depicted the decay of the inner eyewall with a radius of about 50 km, as it
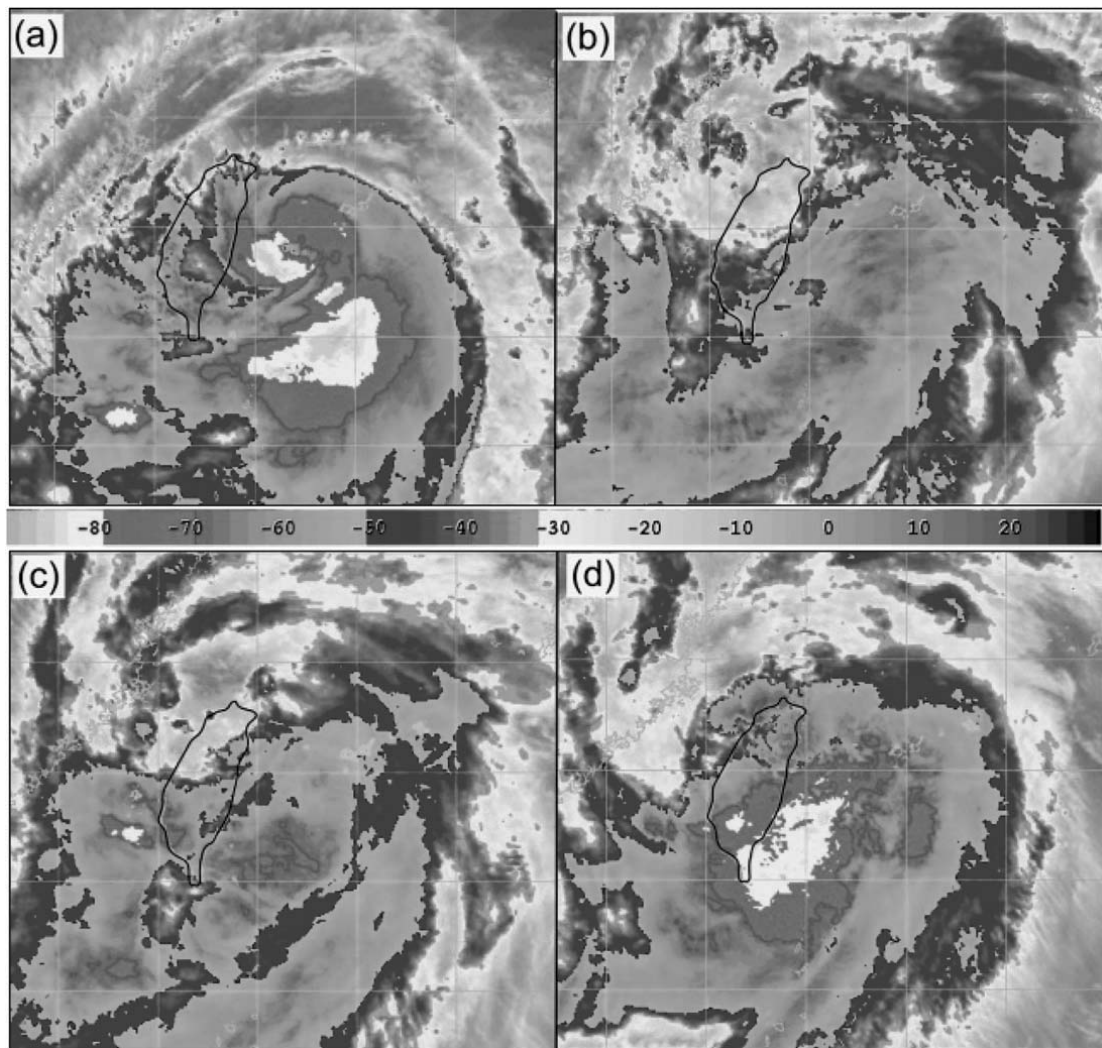
FIG. 4. Enhanced infrared imagery from the geostationary *Multifunctional Transport Satellite* (*MTSAT*) showing cloud-top temperature (°C), at (a) 0030 UTC 7 Aug, (b) 0530 UTC 8 Aug, (c) 0830 UTC 8 Aug, and (d) 1457 UTC 8 Aug 2009.

approached the eastern coast of Taiwan (Fig. 5). As mentioned earlier, this inner eyewall was not well re-solved in the initialization of the model runs, although a local maximum in cyclonic vorticity was located near the center of the inner eyewall, (Fig. 2a, center marked O) for A3_0700T. This inner vorticity maximum weakened and eventually decayed as it moved west and made landfall on the eastern coast of Taiwan in the first 6 h of integration (Fig. 2b), with a similar evolution taking place in other 3-km runs. This weakening was about 12 h slower in the 15-km runs (not shown).

Following the decay of the inner eyewall, the system comprised an annulus of elevated cyclonic vorticity sur-rounding a broad area of weak winds in the center, rep-resenting a new, larger eyewall. This evolution closely resembles that of Typhoon Zeb (1998) over Luzon, as documented in Wu et al. (2009a), although in the

present case, the inner eyewall had mostly decayed prior to landfall, and the outer eyewall had a radius of about 220 km, or nearly twice that of Zeb.

Previous theoretical, modeling, and observational studies have documented the formation of mesoscale waves near the radius of maximum winds in TCs with this type of vorticity annulus structure. Chen and Yau (2001) used the MM5 to simulate an initially axisym-metric vortex, and the model produced potential vorticity (PV) bands consistent with VRW theory (Montgomery and Kallenbach 1997). Wang (2002b) also found that the mesoscale structure in his high-resolution TC model was dominated by WN1 and WN2 VRWs. Crucially, both studies found that VRW structures in the eyewall were well correlated with convection and diabatic heating, suggesting an important role of VRWs in the development of inner spiral bands, and hence rainfall
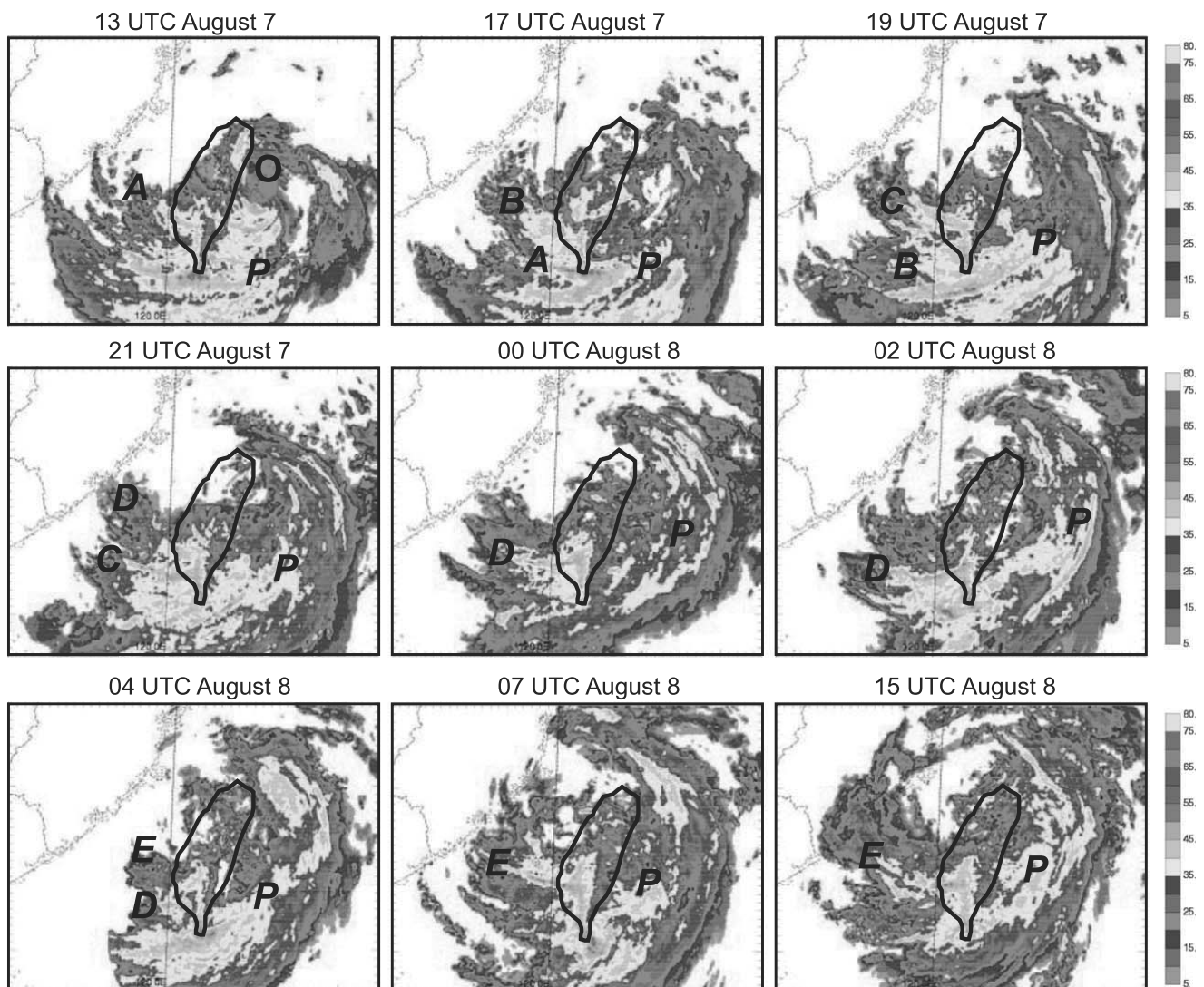
FIG. 5. Mosaic of composite reflectivity (dBZ) from the four CWB Doppler radars with sites shown in Fig. 1. Note the nonuniform time differences between panels. An O denotes the center of typhoon, P the WN1 primary rainband, and A–E outer rainbands associated with VRWs that propagate counterclockwise on the western side within the typhoon vortex.

variability near the center. Observationally, Kuo et al. (1999) and Reasor et al. (2000) described elliptical eyewalls and associated asymmetries in convection in Typhoon Herb and Hurricane Olivia, respectively, although they did not attribute them to VRW activity. Recently, Corbosiero et al. (2006) provided further confirmation of the modeling results, utilizing surface-based radar data collected in Hurricane Elena, and showing that it closely matched structures in the high-resolution model simulations.

In the Morakot simulations, wave structures rapidly developed in the outer eyewall during the first few hours (Fig. 2). The waves had considerable radial amplitude and produced distortions in the annular vorticity structure of the cyclone. To classify these wave structures, their evolution through time and interaction with deep convection in the outer eyewall, a Fourier analysis of relative vorticity was performed in the azimuthal direction by first interpolating the model Cartesian coordinate values to cylindrical coordinates based on the center fix described earlier, and then applying a fast Fourier transform (FFT) in the azimuthal direction. Similar analyses of vertical motion and model reflectivity were performed, but are less relevant to the present case, for reasons elaborated upon below.

The FFT procedure is outlined here. The FFT $\hat{X}_r$ for any parameter x_r at radius r was calculated using

$$\hat{X}_r(k) = \sum_{n=1}^{N} x_r(n) \exp\left[\frac{-i2\pi(k-1)(n-1)}{N}\right] \quad 1 \le k \le N,$$
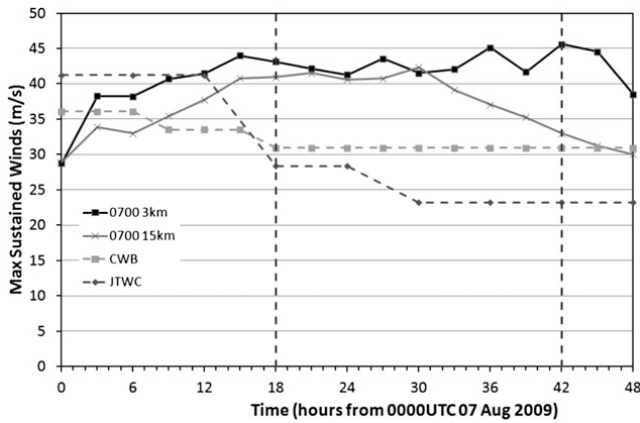
(3)

FIG. 6. Intensity time series for A3_0700T and A15_0700T, with best-track estimates from the CWB and JTWC. Wind speeds are approximate 1-minute sustained at lowest model level that is about 25 m above ground. Dashed vertical line at 18 (42) h indicates observed coastal crossing of the typhoon center on the eastern (western) coast of Taiwan.
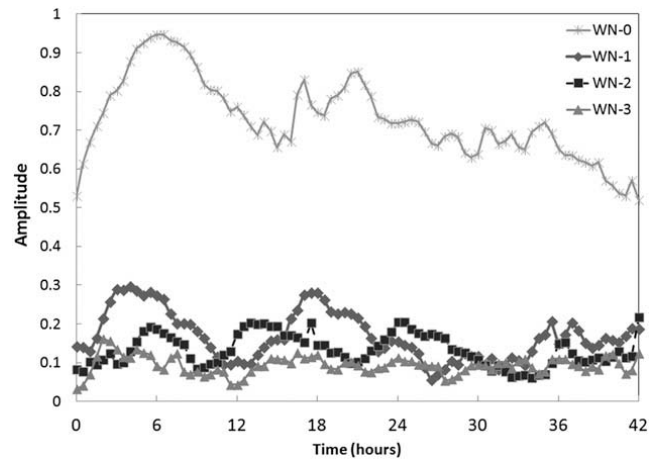

FIG. 7. Amplitude of vorticity components in azimuthal wavenumbers 0 (symmetric flow)–4, through the first 42 h of integration of the A3_0706T model run (10^{-4} s^{-1}).

for each azimuthal wavenumber k, and with N set to 512. In practice, only wavenumbers 0–4 were retained. The amplitude A and phase φ of each parameter at r in frequency space is then given by

$$A_r(k) = \sqrt{\mathcal{R}[\hat{X}_r(k)]^2 + \mathfrak{I}[\hat{X}_r(k)]^2}, \quad \text{and} \quad (4)$$

$$\varphi_r(k) = \mathrm{atan}\{\mathcal{R}[\hat{X}_r(k)], \mathfrak{I}[\hat{X}_r(k)]\}, \quad (5)$$

where $\mathcal{R}[\cdot]$ and $\mathfrak{I}[\cdot]$ are the real and imaginary parts, respectively. From this, the projection of the original parameter onto each wavenumber at each radius is given by

$$\hat{X}_r(k) = A_r(k) \cos[\theta + \varphi_r(k)]. \quad (6)$$

A time series of the amplitude of the low-wavenumber vorticity asymmetries is shown in Fig. 7 for the A3_0706T model run (the maximum vorticity at any radius in the typhoon circulation is shown here, rather than at the radius of maximum winds). As expected, the symmetric flow, represented by WN0, dominated the circulation, being 3–4 times larger than the asymmetric components; it weakened gradually over time as the typhoon lost intensity. Asymmetries generally decreased with increasing wavenumber at most time periods, with WN1 generally having the highest amplitude, although occasionally the WN2 signal was stronger than WN1 for periods of several hours. WN3 was typically slightly weaker, and sometimes only weakly detectable, although occasionally comparable to WN2. These results are similar to the previous studies mentioned earlier (e.g., Chen and Yau 2001; Wang 2002b) and are consistent with Wang (2008) who

showed that the strong deformation associated with the radial shear of the azimuthal flow leads to stronger damping and axisymmetrization of higher-wavenumber anomalies. In this case, there is relatively more power in WN2 and especially WN3 than, for example, in Wang (2002b). This is unlikely to be due to the higher-resolution model used here, as a similar distribution of amplitude amongst the low WNs was found for the 15-km ARPS runs, even though the power in all WNs was less (not shown). It is more likely to be a result of the much larger radius of Morakot, which allows WN3 wavelengths to be larger than the convective scale.

In Fig. 8, a time–azimuth (azimuth is 0° due north and 90° due east) Hovmöller diagram is presented for A3_0700NT, at the radius of maximum winds which varies with time. It shows upward vertical motion for the total field, and low-wavenumber relative vorticity (Note that the total field for vertical motion is shown because the projection of vertical motion onto WN2 is weak, due to the WN1 suppression over the up-shear side of the typhoon, and that the scale is different between panels). The propagation of the WN2 and WN3 VRWs is evident, as is their association with upward motion, particularly in the southern semicircle (azimuths increasing from 90° through 270°). Upward motion develops as individual waves move cyclonically through about 300° azimuth, and subsequently weakens once they reach about 60° azimuth and move into the up-shear side. Propagation of WN1 waves is much less evident, as is the relationship to vertical motion, and is likely related to the persistent WN1 asymmetry induced by the environmental vertical shear over the cyclone. Figure 8b indicates a persistent anticyclonic WN1 anomaly on the southern side, as the shear-induced WN1 anomaly tends to be located at a smaller radius, well inside the radius
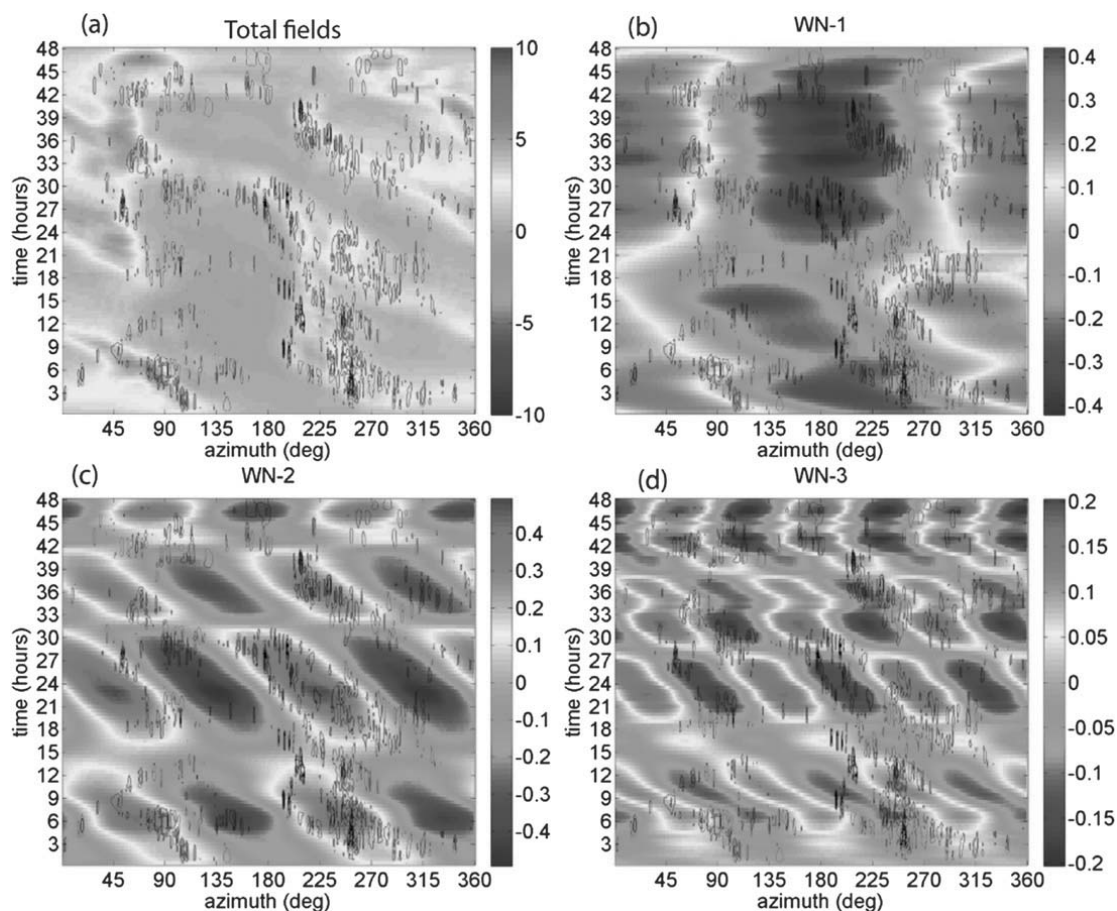
FIG. 8. Time–azimuth Hovmöller plots of relative vorticity (shaded, 10^{-4} s^{-1}) and vertical motion (contoured, interval 0.6 m s^{-1}; only upward motion shown and no zero contour) for the A3_0706NT run showing (a) the total field, and wavenumber (b) 1, (c) 2, and (d) 3 of vorticity. Note that vertical motion is the total field, repeated in each panel, and that the shading scale is different between panels. Radius varies slightly with time and is set to the radius of maximum winds.

of maximum winds used to construct Fig. 8. A typical example is Fig. 9, where stronger winds in the southeastern quadrant associated with the persistent deep convection provide a WN1 structure, also obvious in its associated vorticity field. This observation is consistent with previous studies of convective organization in relation to vertical shear (Braun and Wu 2007). In this case, the environmental vertical shear of the 200–850-hPa layer was generally north–northeasterly averaging around 12–14 m s^{-1} prior to landfall over Taiwan which, from Fig. 9b, is consistent with most deep convection being located in the southeastern quadrant of the system; that is, downshear and downshear left. This strong WN1 asymmetry almost completely suppressed upward motion on the northern side of the cyclone, so WN2 and WN3 asymmetries in vertical motion were weaker in this period.

Further analysis of the azimuthal waves showed a close resemblance to those in Wang (2002b) in vertical structure, with the asymmetric vorticity and vertical motion associated with the waves sloping radially outward

with height (not shown). The phase velocity of the waves was consistent with the analytical VRW theory. Inspection of Fig. 8 reveals that individual WN2 VRWs complete an orbit of the center in about 25 h, and given a mean radius of about 230 km, the ground-relative phase speed is about 16 m s^{-1}, or 55% of the mean tangential wind at that radius. The phase speeds of the WN3 waves are more variable but are slightly slower than those of WN2. These results are similar to previous work and show that there was flow-relative upstream propagation of individual waves, consistent with VRW theory, but the phase speeds relative to the mean flow are somewhat larger in our case. For example, Corbosiero et al. (2006) found that WN2 waves propagated at about 70% of the mean tangential wind speed in Hurricane Elena. Using their method to calculate the phase speed from the dispersion relationship of Möller and Montgomery (2000) yields a ground-relative value of about 20 m s^{-1} for the present case, roughly consistent with but slightly faster than the waves observed in the model. This is an
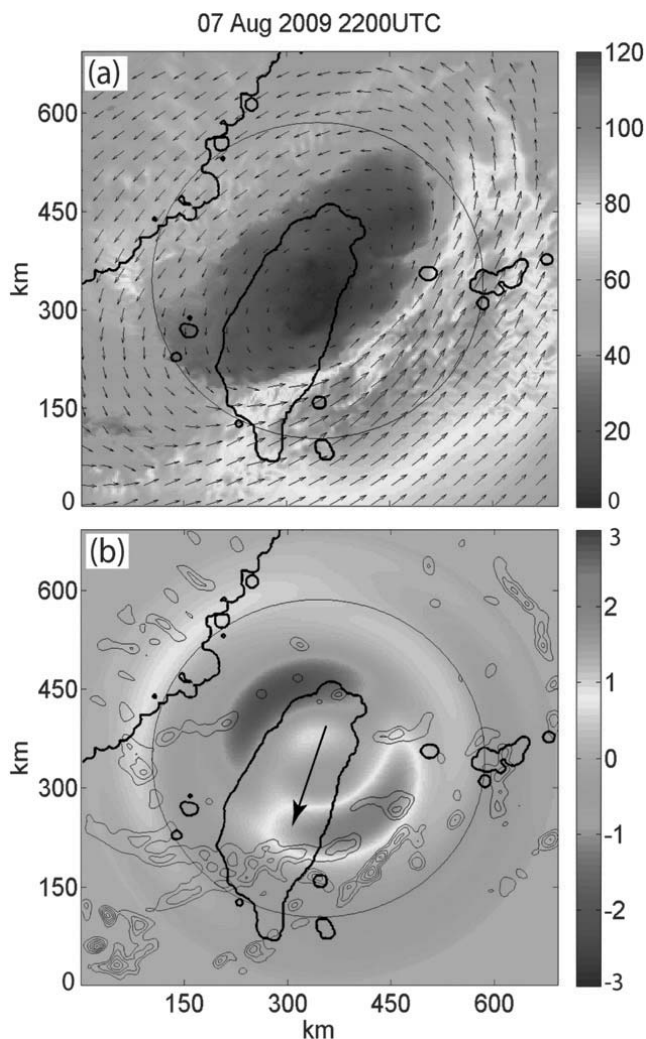
07 Aug 2009 2200UTC

FIG. 9. (a) Horizontal winds (knots; 1 kt = 0.51 m s^{-1}) at approximately 850 hPa, and (b) wavenumber-1 component of relative vorticity (shaded, 10^{-4} s^{-1}) and vertical motion (contoured, interval 0.5 m s^{-1}; only upward motion shown and no zero contour) for the A3_0706NT run. Black circles indicate the radius of maximum winds, the radius used for the Hovmöller plot in Fig. 8, while the black arrow in (b) indicates direction of 850–200-hPa vertical wind shear (magnitude 12 m s^{-1} at this time).

intriguing finding as it is consistent with the observational study of Corbosiero et al. (2006) for Hurricane Elena, but not with the modeling study of Wang (2002b). The obvious possible factor is that of diabatic heating associated with deep convection, neglected in the idealized study by Möller and Montgomery (2000). However, diabatic heating typically would be expected to have the opposite effect on phase speed, according to the PV budget analysis performed in Wang (2002b) because that analysis indicates that the diabatic heating terms tend to oppose the upstream propagation of the waves. Replicating this PV budget analysis, based on Wang's Eq. (5), for the present case, using a 3-km run

with full terrain, revealed that the persistent, intense deep convection in the up-slope flow over southern Taiwan led to an earth-relative slowing of the WN2 VRWs through the asymmetric diabatic heating term. This appears to be the most likely cause of the apparent discrepancy. We will present details on the PV budget diagnostics in a separate paper.

In the radial direction, the stronger waves generally propagated outward and reached a stagnation radius at about 350 km (not shown), which is also consistent with theoretical and observed behavior of VRWs demonstrated in previous studies (e.g., Montgomery and Kallenbach 1997; Wang 2002b; Corbosiero et al. 2006). All evidence indicates that these waves can be identified as VRWs and will henceforth be referred to as such. The relationship between the VRWs, vertical motion and deep convection was complicated by the persistent, vertical shear–induced WN1 asymmetry, which masked the effects of the WN2 and WN3 VRWs in the upshear side of the cyclone. For this reason the projection of these fields onto wavenumbers higher than 1 tended to be weak, and the Fourier analysis was of limited value.

In Fig. 10, the evolution of vertical motion associated with WN2 VRWs from the A3_0706NT model run over a period of three hours is presented. Similar to Fig. 8, a run with no terrain is shown, to emphasize the influence of the waves on vertical motion, and total vertical motion is shown because, as mentioned, the projection onto WN2 tended to be weak because of the WN1 upshear suppression. First, the WN1 asymmetry in vertical motion induced by the vertical shear is clear, especially within the principal rainband stretching from the eastern quadrant of the cyclone to the south of Taiwan. Also prominent is the development of upward motion associated with the VRW approaching southern Taiwan, mainly just downstream and radially outwards from the cyclonic vorticity associated with the approaching wave (Fig. 8). However, the lack of coherent vertical motion associated with its counterpart WN2 wave to the northeast (around 45° azimuth) of Taiwan also can be seen.

The role of VRWs in the development of convective banding on the southwestern side of Morakot is illustrated in Fig. 11. The period shown corresponds to that displayed in Fig. 10, although in this case the Taiwan terrain is in place. The WN1 vorticity asymmetry is mostly associated with the principal rainband, marked P in Fig. 11, which at this time was brushing the far southern tip of Taiwan. At the same time, the WN1 anomaly east of Taiwan near the downwind end of the principal rainband weakens as it moves cyclonically into the upshear part of the cyclone. The WN2 vorticity asymmetry, marked A near southwestern Taiwan,
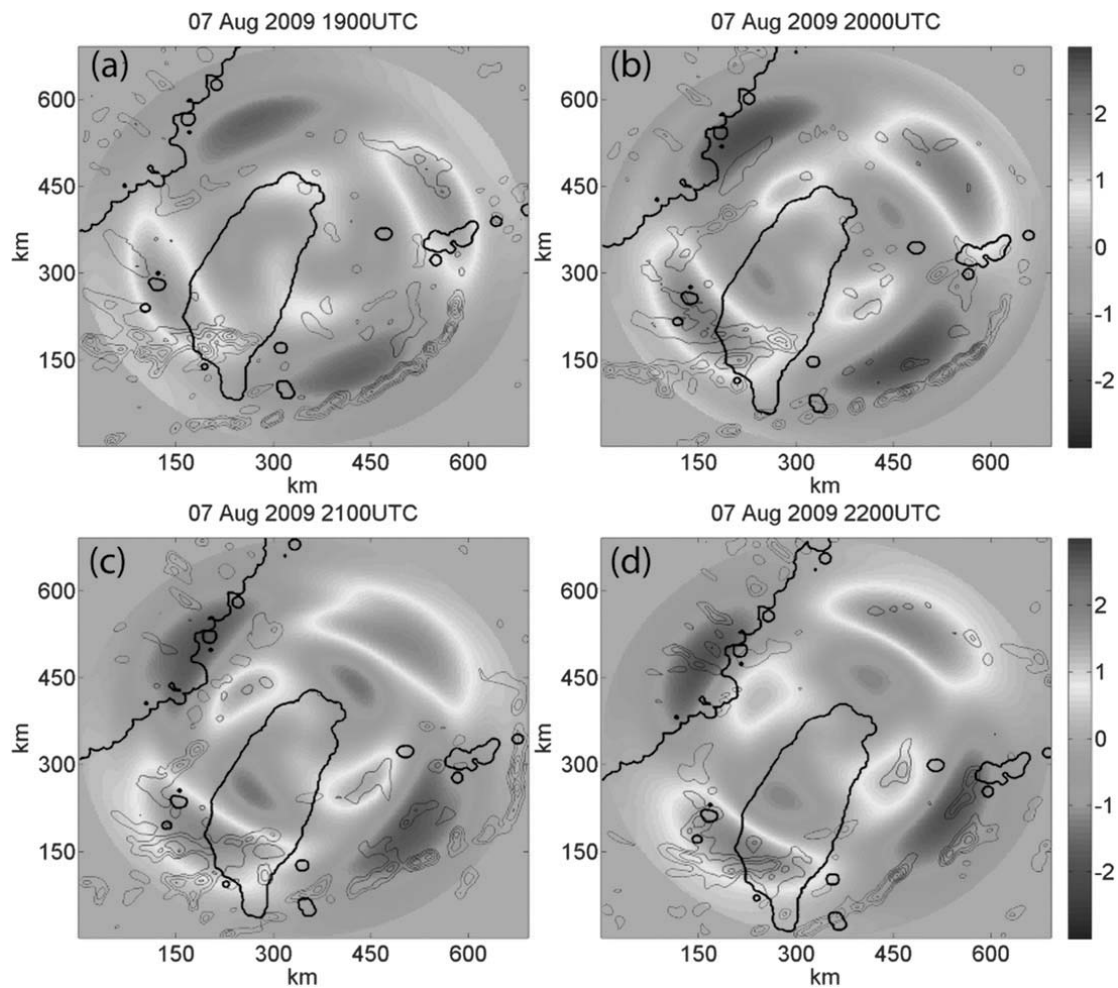
FIG. 10. Wavenumber-2 relative vorticity (shaded, 10^{-4} s^{-1}) and full vertical motion (contoured, interval 0.2 m s^{-1}) at approximately 850 hPa at 1-h interval for A3_0706NT, from (a) 1900 to (d) 2200 UTC 7 Aug 2009.

appeared to be associated with the development of the secondary rainband in this area, and subsequently this band rotated southward with the motion of the VRW. The convergent area evident in the asymmetric winds also moved southward with the motion of this wave.

As noted earlier, the typhoon became almost devoid of vigorous deep convection for several hours while located over Taiwan (Fig. 4b). This period lasted until about 0500 UTC 8 August, following which zonally oriented bands of deep convection redeveloped over the Taiwan Strait to the west of the island in the southwestern quadrant of the TC. The 3-km model runs also featured the recurrent development of these deep convective bands. This is seen in Fig. 12, which is similar to Fig. 11 but is 7 h later. During the interim, the principal rainband (P) remained virtually stationary, lying just south of Taiwan. Also, the band marked A from Fig. 11 had rotated south and merged with the principal band during this time, while another strong convective band, marked

B in Fig. 12, had developed in its place. Also seen at an earlier stage of development is band C, which eventually developed into a mature secondary band as it rotated southward. These developments are like those in the CWB radar imagery in Fig. 5. Here, the near stationary nature of the principal rainband is confirmed for the approximately 24-h period shown, while the development and southward motion of secondary convective bands associated with propagating VRWs near western Taiwan are visible (labeled A, B, C, D, and E in Fig. 5). The development of zonally oriented convective bands over the Taiwan Strait is similar to the case of Typhoon Mindulle (2004) as documented in Lee et al. (2008) and Chien et al. (2008), although here we attribute the enhanced convergence to VRW activity, rather than a secondary circulation center in the case of Mindulle.

To illustrate that these developments occurred virtually independently of topographical forcing, a similar sequence from the A3_0706NT run is shown in Fig. 13.
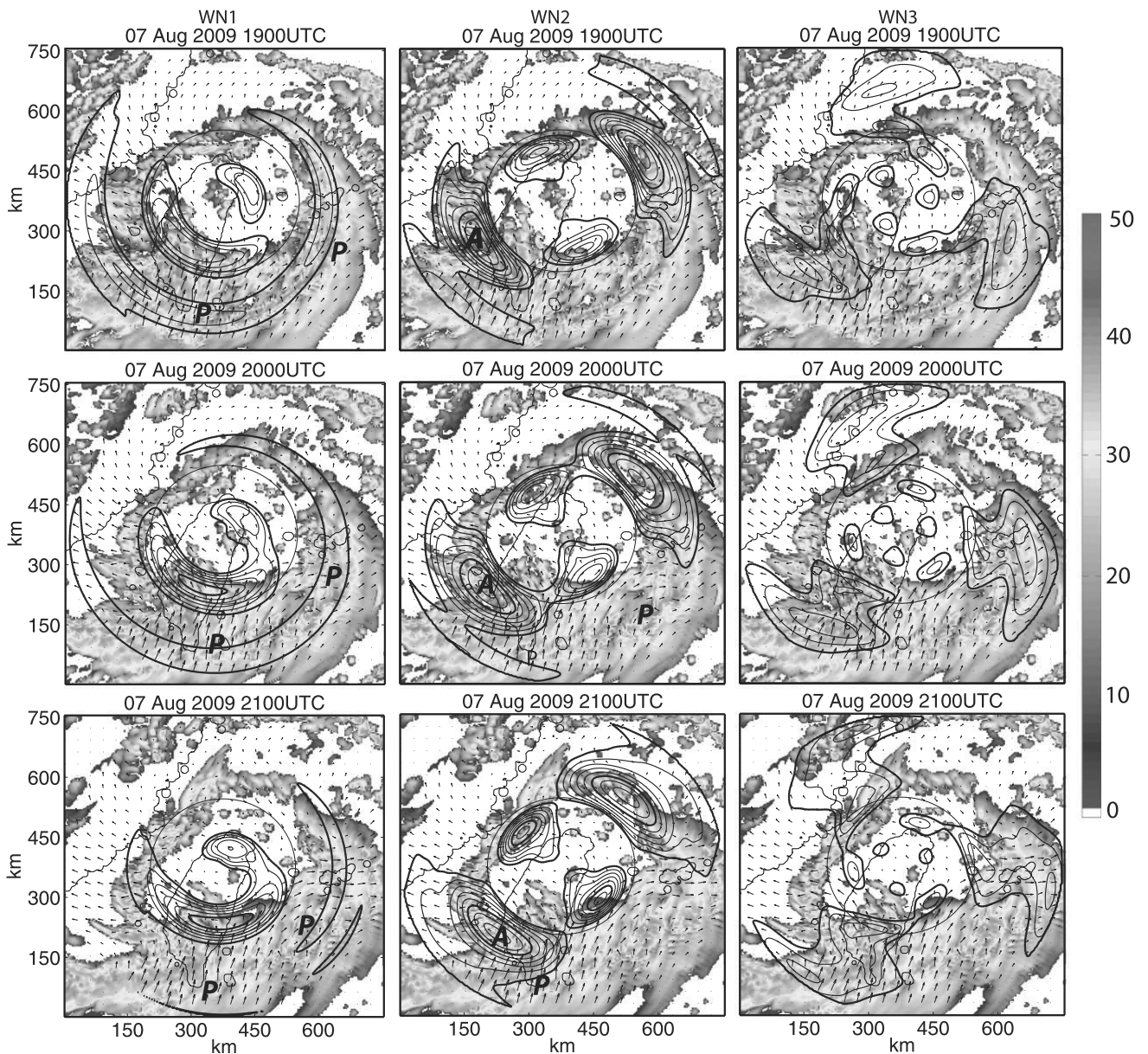
FIG. 11. Model composite reflectivity (shaded, dBZ), asymmetric relative vorticity at approximately 850 hPa, in wavenumbers 1, 2, and 3 (contour, interval 0.2 m s^{-1}; only cyclonic vorticity shown and zero contour omitted), and asymmetric winds (vectors, maximum vector 15 m s^{-1}) for A3_0706T. Asymmetric winds were produced by subtracting mean azimuthal and radial winds. (top) 1900, (middle) 2000, and (bottom) 2100 UTC 7 Aug 2009. Features labeled with italic capital letters (P, A, etc.) are explained in the text.

Here it can be seen that the structure of the convective bands and their positions relative to the VRWs are very similar to the full-terrain case, although the timing is slightly different. In particular, the association between the band labeled A and the WN2 VRW is clear, and very reminiscent of the full terrain case. The separation from the principal rainband, labeled P, is similarly clear. Not surprisingly, this leads to a similar pattern of accumulated rainfall between the terrain and no-terrain cases in the area upstream from the Taiwan mountains, as will be shown in section 4 below.

There appears to be an association between WN2 and WN3 waves and reflectivity bands in the 3-km model runs in the northern part of the cyclone at the later time shown in Fig. 12, consistent with the weakening vertical shear over the system at this time. Again there is observational evidence of this increasing symmetry, in the radar imagery. It is also evident that the major secondary bands are more closely associated with WN2 waves, suggesting that they were more important than WN3 in the organization of convective bands in this scale.
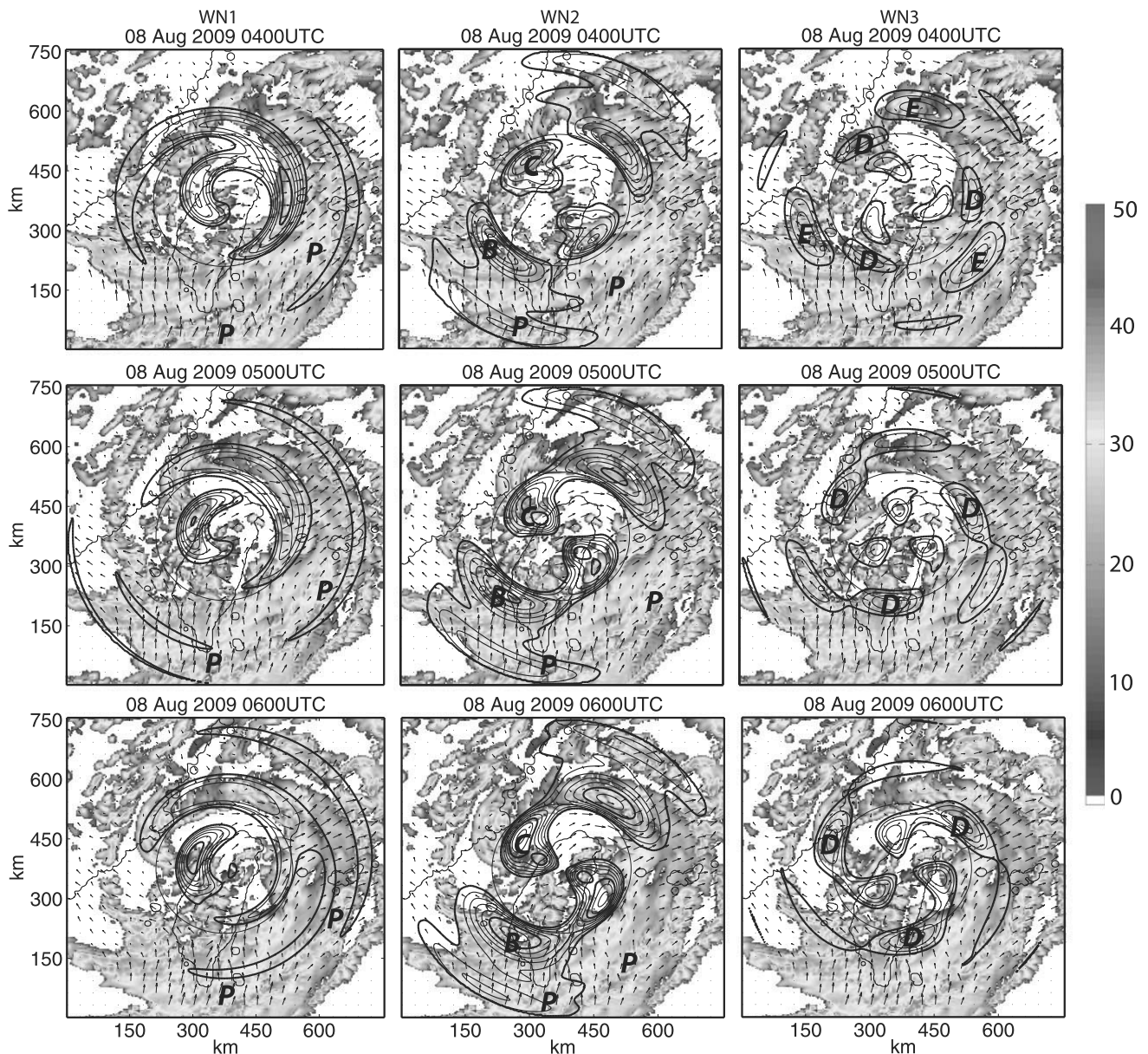
FIG. 12. As in Fig. 11, but for (top) 0400, (middle) 0500, and (bottom) 0600 UTC 8 Aug 2009.

The results are consistent with those reported by Braun et al. (2006) and Braun and Wu (2007) in their simulations of Hurricanes Erin and Bonnie, and conform to their conceptual model of the interaction of vertical shear, vertical motion and mesoscale waves near the eyewall (their Fig. 18), although the fact that WN2 and WN3 waves are of similar amplitude in Morakot complicates the relationship between asymmetric vorticity and upward-motion leading to deep convection. The convective bands on the western flank of the Morakot played an important role in the location and intensity of the extreme rainfall, particularly as the downstream (eastern) end of the bands interacted with the western slopes of the Taiwan CMR.

4. Model rainfall and verification against observations

a. Rainfall evolution

Previous studies of Morakot, cited in the introduction, have documented the broad-scale influences leading to the heavy-rainfall episode over Taiwan. Additionally, Lin et al. (2010) and Chien and Kuo (2011) emphasized the role of the relatively slow motion of the cyclone, the very moist southwesterly monsoon flow, and broad-scale convergence of this flow with the western flank of Morakot's circulation. They attributed these factors, together with orographic lift along the western slopes of the CMR, as primary causes of the extreme rainfall.
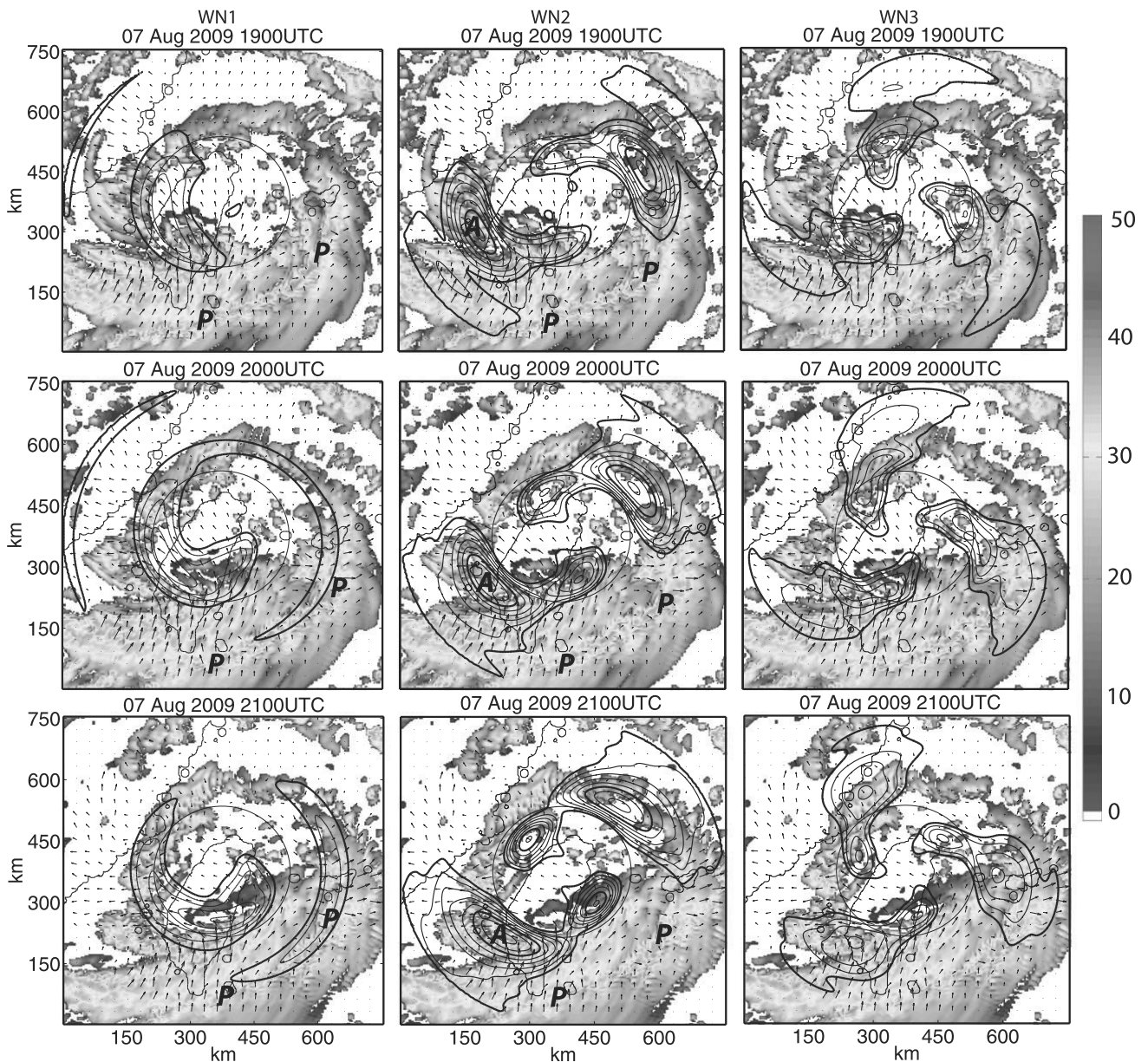
FIG. 13. As in Fig. 11, but for 3-km run A3_0706NT without terrain.

The current study suggests that, in addition to the broad convergence of the monsoon southwesterly flow on the southern flank of the typhoon, and the topographic effects of the CMR, VRW activity in the outer eyewall of Morakot played an important role in organizing and focusing the development of deep convective bands on the western flank of the typhoon, which also interacted with the CMR. Early in the period, when Morakot had a predominantly westward track, these bands moved southward in both a TC- and earth-relative sense due to the cyclonic azimuthal flow on the western side of the TC. This evolution is seen in Fig. 5 for bands A, B, and C. However, later in the period as Morakot

adopted a more northward track, the bands were almost stationary in an Earth relative sense (band D in Fig. 5), as the motion of the typhoon tended to cancel the cyclonic rotation of the bands around the center, assisted by the upstream propagation of the VRWs. The slowing of the earth-relative motion of these deep convective bands appears to play an important role in focusing their influence and rainfall over specific parts of the CMR, and in determining the extreme rainfall accumulations for the event, in addition to the lifting effect of the CMR.

The topographic enhancement of rainfall in specific sections of the CMR was examined by Lin et al. (2002) and Chiao and Lin (2003), using the ingredients-based
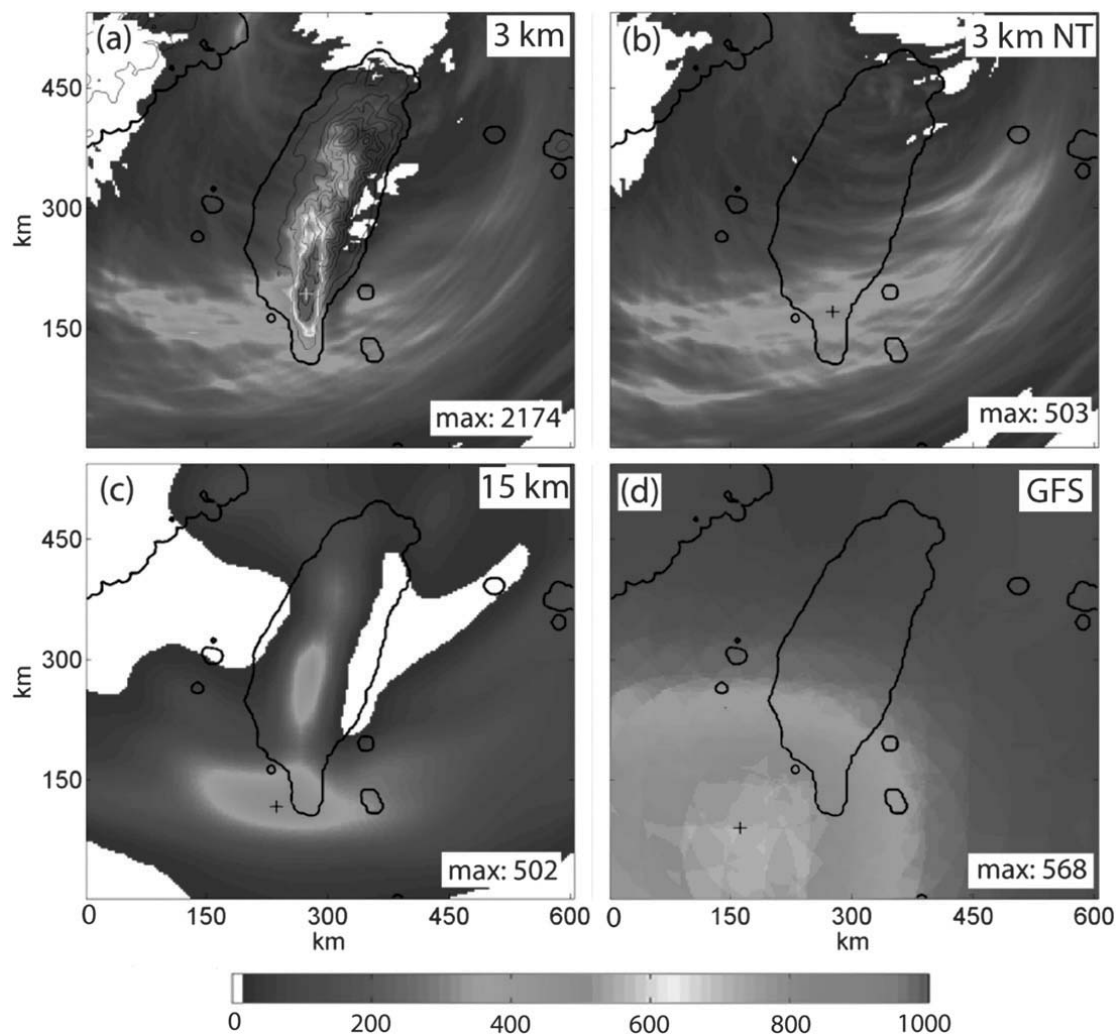
FIG. 14. Accumulated rainfall (mm) for the 36-h period 1200 UTC 7 Aug–0000 UTC 9 Aug 2009, for (a) A3_0700T; (b) A3_0700NT; (c) A15_0700; and (d) GFS_0700. The 3-km model topography is shown in (a) with a contour interval of 200 m. Maximum rainfall in this period is shown in the lower-right corner of each panel, at positions marked with a plus sign [the plus sign in (a) is a lighter shade for clarity].

approach of Lin et al. (2001). The latter identified a group of processes that can be thought of as ingredients in the development of a heavy topographically induced rainfall event. In particular, they suggest that a heavy topographic-rainfall event requires significant contributions from any combination of the following ingredients: 1) a high precipitation efficiency of the incoming airstream; 2) a low-level jet; 3) a steep mountain; 4) high moisture upstream; 5) favorable mountain geometry (such as a concave geometry) and a confluent flow field; 6) strong synoptically forced upward vertical motion; 7) a large convective system; 8) slow movement of the convective system; and 9) a conditionally or potentially unstable airstream upstream. For Morakot, many of these ingredients were in place along the western coast of Taiwan through much of the event. There was a large, slow moving convective system in an environment of high

moisture content, represented by the convective bands described above, and the steep western slopes of the CMR provided the third ingredient. Interestingly, the VRW-induced convective bands are also associated with a low-level wind maximum, which increases the topographic forcing through ingredient 2 as it impinges on the CMR.

The total rainfall accumulations for the 36 h to 0000 UTC 9 August from 3-km full-terrain and no-terrain, 15-km, and GFS runs are shown in Fig. 14. Both 3-km runs show a banded precipitation pattern upstream of the CMR, although the long accumulation time masks the details. In Fig. 15, a shorter accumulation period of 6 h is shown for two separate periods from the A3_0706T and A3_0706NT runs. Here, the banded features near the western coast of Taiwan are clearer in both the terrain and no-terrain runs, and show the effects of the deep
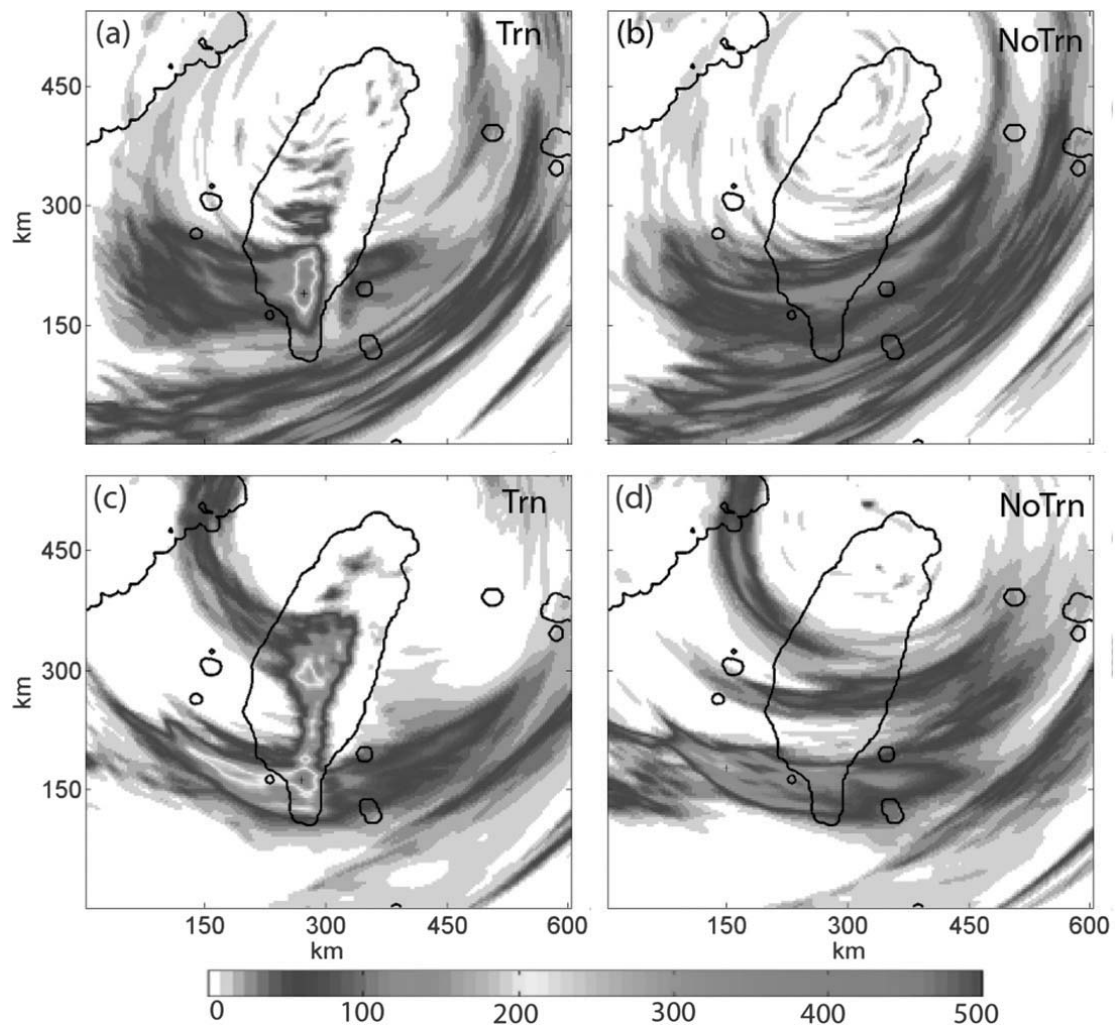
FIG. 15. 6-h rainfall accumulations (mm) for (a),(c) 0100–0700 UTC 4 Aug 2009 from A3_0706T and (b),(d) 1100–1700 UTC 4 Aug 2009 from A3_0706NT.

convective bands associated with VRWs mentioned in the previous section. The main effect of terrain appears to be the local focusing of deep convection and enhancement of rainfall when these bands impact the western slopes of the CMR, and also the rain-shadow effect of low rainfall on the lee (eastern) side of the mountain range over southern Taiwan. These results are supported by the radar-derived quantitative precipitation estimates (QPE) for the same periods, as shown in Fig. 16. Despite the presence of some bright-banding, particularly to the northeast of Taiwan, and local sea clutter near the radars, the radar QPE is useful for qualitative verification of the model results. Noteworthy is that both the 3-km model and radar QPE observations show a similar separation between the bands of precipitation, although the orientation of the bands differ slightly, primarily due to the model's tendency to move the typhoon too quickly to the north (Fig. 3).

The 15-km ARPS runs also produced weaker VRWs, and even weaker secondary convective banding, and a similar rainfall pattern is produced to the higher-resolution runs (Fig. 14c), although peak totals were less than half as large. Higher rainfall amounts were associated with the principal rainband near the far southern tip of Taiwan, in the broad convergent zone between the monsoon southwesterlies and the mean circulation of the TC. Such a process was emphasized by Ge et al. (2010). In the even-lower-resolution GFS global model, VRWs were not resolved, the secondary banding did not develop, and there is no rainfall peak over central southern Taiwan. For this model, the peak rainfall occurred even further south and again was associated with the principal TC rainband.

The timing of the onset of heavy to extreme rainfall is an important practical consideration, especially for possible evacuations. The 3-km ARPS runs consistently
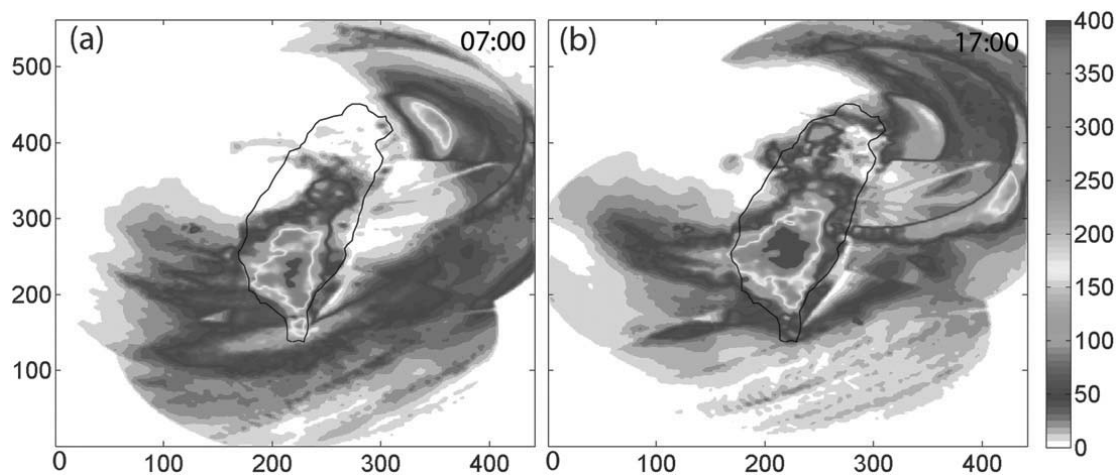
FIG. 16. 6-h radar-estimated rainfall accumulations corresponding to the two periods shown in Fig. 15.

forecast the onset of hourly rain rates above 60 mm h^{-1} over the western slopes of the CMR between about 1600 and 1800 UTC 7 August, coinciding with rain gauge observations. The ARPS 3-km runs produced peak hourly rainfall rates of about 110 mm h^{-1}, close to the observed rain gauge peaks (not shown).

b. Precipitation forecast verification

To quantitatively assess the quality of the ARPS rainfall forecasts for the Morakot event, they were verified against the rain gauge analysis from the Taiwan CWB for the 36-h period from 1200 UTC 7 August to 0000 UTC 9 August, which constituted the main part of the rainfall event, and it is the period shown in Fig. 14 for the model results. The rain gauge analysis from the CWB was interpolated onto the 3-km ARPS grid using a single-pass Barnes interpolation, and is shown in Fig. 17.

Quantitatively, because the main interest in this study is the location and storm total amounts of the extreme rainfall, the spatial correlation coefficient was calculated, along with the equitable threat score (ETS) (Schaefer 1990), which is a measure of how well the forecast and
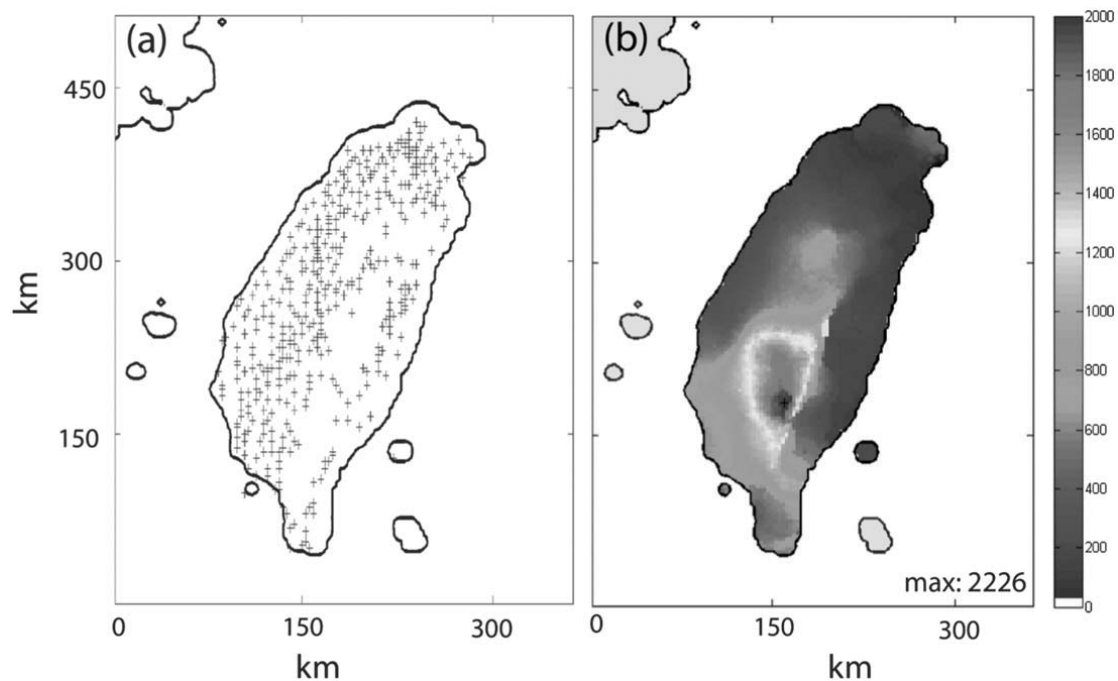

FIG. 17. (a) The hourly automatic rain gauge network over Taiwan used in (b) the total accumulated rainfall (mm) for the 36-h period 1200 UTC 7 Aug–0000 UTC 9 Aug 2009. Maximum rainfall is indicated in the lower-right corner of (b), at the position marked with a plus sign.

TABLE 3. Verification statistics of rainfall accumulations for the 36-h period 1200 UTC 7 Aug–0000 UTC 9 Aug 2009, for amounts above four different rainfall thresholds. ETS is equitable threat score, POD is the probability of detection, FAR is false alarm ratio, and BIAS is the bias. Where a model run does not produce any rainfall above a particular threshold, it is omitted from the table.

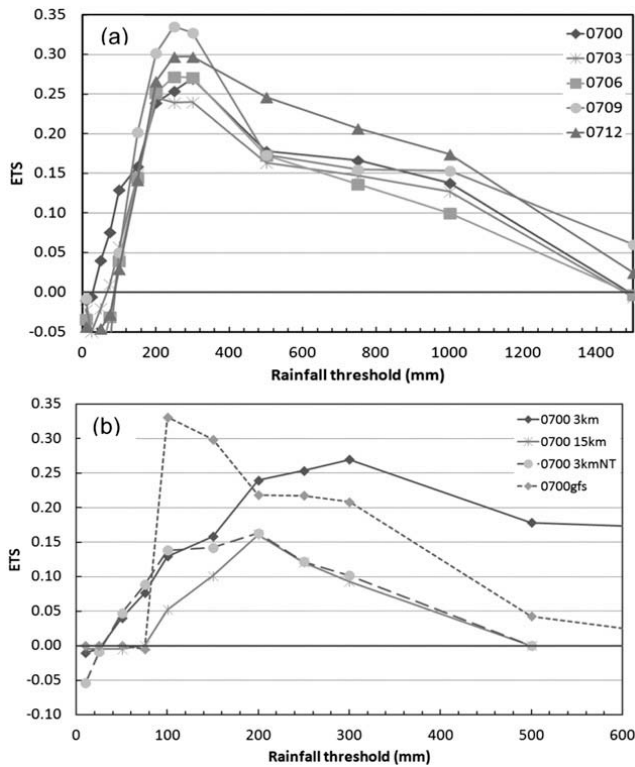| Model	Threshold (mm)	ETS	POD	FAR	BIAS
A3_0700T	150	0.158	0.504	0.077	0.546
A3_0709T	150	0.202	0.568	0.065	0.608
GFS	150	0.299	0.704	0.067	0.754
A3_0700NT	150	0.092	0.354	0.085	0.387
A15_0700	150	0.142	0.417	0.032	0.431
A3_0700T	300	0.270	0.464	0.042	0.484
A3_0709T	300	0.328	0.513	0.003	0.514
GFS	300	0.208	0.430	0.129	0.493
A3_0700NT	300	0.084	0.200	0.136	0.232
A15_0700	300	0.102	0.210	0.059	0.223
A3_0700T	500	0.178	0.267	0.022	0.273
A3_0709T	500	0.173	0.265	0.043	0.277
GFS	500	0.042	0.078	0.160	0.092
A3_0700T	1000	0.138	0.177	0.324	0.262
A3_0709T	1000	0.153	0.195	0.307	0.282

FIG. 18. ETSs from various model runs for rainfall thresholds over the 36-h period 1200 UTC 7 Aug–0000 UTC 9 Aug 2011. ETS is calculated over land areas of Taiwan using CWB hourly rain gauge analysis. (a) For ARPS 3-km runs with terrain, and (b) runs commencing at 0000 UTC 7 Aug 2009 from ARPS 3-km with and without terrain, ARPS 15 km, and GFS.

observed fields match, for amounts above a given threshold. Here, the ETS was calculated for 14 rainfall thresholds ranging from 10 to 2000 mm. Figure 18a shows that the 3-km runs with terrain provided skillful guidance of total rainfall, even at large thresholds between 1000 and 1500 mm. Comparison of the total rainfall forecast of Fig. 14a with the gauge analysis in Fig. 17b, where the principal error in the forecast has the peak rainfall slightly too far south. Thus, the model overforecasts for far southern Taiwan, and underforecasts near the actual peak in the Alishan area (although rainfall amounts near 1000 mm were predicted in this area). Generally, the latest run, A3_0712T, is the most skillful above 200 mm, probably due to its improved track forecast late in the period, rather than a better representation of the mesoscale structure of the cyclone. The earlier 3-km runs had similar tracks, and the results are closely clustered for all thresholds.

In Fig. 18b, comparison is made among precipitation forecasts of the two ARPS 3-km runs with and without terrain, the ARPS 15-km run (with terrain), and the GFS forecast. For all precipitation totals except for 100 and 150 mm, the 3-km run with terrain produces the best

ETS scores, with the 3-km run without terrain producing similar scores for thresholds up to 150 mm. The loss of skill for higher thresholds in the 3-km run without terrain points to the important contributions of terrain interactions to heavy precipitation. The 15-km ARPS run produces generally poor ETS scores; this appears to be related to its poor track forecast (c.f., Fig. 3a). GFS shows poor skill scores for high thresholds, indicating its inability to resolve VRW structures or the orographic forcing. For thresholds of 100 and 150 mm, GFS however shows the highest ETSs among all runs; this may be due to the reasonable ability of well-tuned cumulus parameterization schemes in coarse-resolution models in capturing lighter precipitation, and relatively poor performance of convection-permitting models relying on a single moment microphysics parameterization scheme in accurately capturing stratiform precipitation (e.g., Bryan and Morrison 2011).

These results are further quantified in Table 3, where the ETS, probability of detection (POD), false alarm ratio (FAR) and bias (BIAS) are shown for four key rainfall thresholds for selected model runs. Definitions of these parameters can be found in Wilks (2006). Overall, each model displayed a low bias at the thresholds shown. Typically, the bias should be insensitive to forecast track errors, but the relatively small verifying domain in this case means that track errors may be significant. At the 150-mm threshold where the GFS has the higher ETS, it has the best POD and a similar FAR to other models but has a smaller bias. Above the 300-mm threshold, the 3-km ARPS runs become superior in all

measures, with POD remaining near 0.5 and very low FAR. Given significant rainfall in the lead-up to the event, this threshold is likely to be significant for the development of landslides and debris flows in the CMR (e.g., Jan et al. 2007). At higher thresholds, the effect of the placement of organized convection becomes more important, with decreasing POD and increasing FAR in the 3-km runs; however, useful skill even at 1000 mm is encouraging. The low bias and POD of the A3_0700NT relative to the other runs explains much of its poor performance, and indicates that topographic enhancement is important, even at relatively low rainfall rates.

5. Summary and conclusions

In this study, a successful attempt was made to simulate the Taiwan landfall phase of Typhoon Morakot using the ARPS high-resolution nonhydrostatic mesoscale model, with initialization from operational global model analyses. Significant outcomes are as follows.

(i) ARPS runs with a 3-km grid spacing accurately reproduced the track of Morakot during the landfall phase over Taiwan, for forecast lead times from 3 to 12 h, although they moved the cyclone to the north too quickly later after landfall. ARPS simulations at 15-km grid spacing produced tracks that incorrectly deflected northward before landfall, presumably owing to the smaller radius of maximum wind in the simulation that interacts with Taiwan terrain before landfall. There was little variation in tracks between runs with and without Taiwan terrain, suggesting little topographic influence on the cyclone's motion in this case, likely because of the large size of Morakot relative to the Taiwan Island.

(ii) The 3-km ARPS runs developed mesoscale wave structures in the outer eyewall consistent with satellite and radar imagery of the event, and closely resembling vortex Rossby waves (VRWs) identified in previous modeling and observational studies. Similar VRW structures were also found in 3-km runs with Taiwan terrain set to zero, implying that terrain forcing was not responsible for the waves.

(iii) The cyclone has a persistent wavenumber-1 (WN1) asymmetry, with convection confined entirely to the southern semicircle, consistent with the moderate to strong northeasterly vertical shear over the system (Figs. 4 and 5). WN2 and WN3 also had significant amplitudes, though generally smaller than WN1. As WN2 and WN3 VRWs developed and moved cyclonically around the outer eyewall, the upward vertical motion associated with them was suppressed over the northern (upshear) side but redeveloped as the waves propagated into the downshear (southern) side of the cyclone.

(iv) As shown in Figs. 5, 11, and 12, there appear to be three main processes controlling the distribution of extreme rainfall. They are the following: 1) the almost stationary WN1 convective band near the southern tip of Taiwan, associated with the vertical shear over the system and broad scale convergence between the vortex circulation and the southwesterly monsoon flow; 2) the development of secondary bands of deep convection associated with VRWs, as outlined in section 3; and 3) the local-scale enhancement of rainfall from up-slope flow into the CMR, particularly when enhanced by the convective bands. The complete model runs had two to three separate episodes of secondary convective band development associated with process 2 over the 36–48-h period of the runs. The precise location of the convective outbreaks varied slightly between the runs, depending on the track of the cyclone and the timing of the development of VRWs. Combined with the interaction of the convective bands with the CMR, the location of the peak rainfall over Taiwan was affected. The operational GFS runs with coarser resolution did not resolve the VRWs, and thus was not able produce the secondary convective bands associated with the VRW activities. Consequently, the rainfall peak from this model was farther south, associated with process 1, of the principal rainband. It can be concluded that although the track of the cyclone is of primary importance, and topographic enhancement played a critical role in the extreme rainfall produced, the mesoscale organization of deep convection by the environmental vertical shear and VRWs also had important effects on the topographic enhancement itself, and on the overall spatial and temporal rainfall distribution.

(v) The 3-km model runs produced useful skill in predicting rainfall accumulations for the event, measured by equitable threat scores, especially for threshold values between 500 and 1500 mm in the 36 h from 0012 UTC 7 August to 0000 UTC 9 August 2009 (Fig. 18). Although the coarse-resolution operational GFS model can produce reasonable QPF skill at low rainfall thresholds, it cannot provide guidance to higher-intensity rainfall patterns produced during the event since it does not capture the organization of deep convection, or persistent near-stationary convection associated with the upslope flow into the CMR.

This study shows that a high-resolution model, in this case the ARPS model, can provide valuable guidance for a complex, high-impact event such as Morakot. In particular, the model was able to resolve features such as VRWs that likely exert significant control over the timing and placement of deep convective bands. This study presented evidence of VRWs in the high-resolution simulations and confirmed their important role in determining the locations of heavy precipitation in Typhoon Morakot. These are aspects not discussed in previously published studies on Morakot.

REFERENCES

Atallah, E. H., and L. F. Bosart, 2003: The extratropical transition and precipitation distribution of Hurricane Floyd (1999). *Mon. Wea. Rev.,* **131,** 1063–1081.

Braun, S. A., and L. Wu, 2007: A numerical study of Hurricane Erin (2001). Part II: Shear and the organization of eyewall vertical motion. *Mon. Wea. Rev.,* **135,** 1179–1194.

——, M. T. Montgomery, and Z. Pu, 2006: High-resolution simulation of hurricane Bonnie (1998). Part I: The organization of eyewall vertical motion. *J. Atmos. Sci.,* **63,** 19–42.

Bryan, G. H., and H. Morrison, 2011: Sensitivity of a simulated squall line to horizontal resolution and parameterization of microphysics. *Mon. Wea. Rev.,* **140,** 202–225.

Burpee, R. W., and M. L. Black, 1989: Temporal and spatial variations of rainfall near the centers of two tropical cyclones. *Mon. Wea. Rev.,* **117,** 2204–2218.

Chen, Y., and M. K. Yau, 2001: Spiral bands in a simulated hurricane. Part I: Vortex Rossby wave verification. *J. Atmos. Sci.,* **58,** 2128–2145.

——, G. Brunet, and M. K. Yau, 2003: Spiral bands in a simulated hurricane. Part II: Wave activity diagnostics. *J. Atmos. Sci.,* **60,** 1239–1256.

Chiao, S., and Y.-L. Lin, 2003: Numerical modeling of an orographically enhanced precipitation event associated with tropical storm Rachel over Taiwan. *Wea. Forecasting,* **18,** 325–344.

Chien, F.-C., and H.-C. Kuo, 2011: On the extreme rainfall of Typhoon Morakot (2009). *J. Geophys. Res.,* **116,** D05104, doi:10.1029/2010JD015092.

——, Y.-C. Liu, and C.-S. Lee, 2008: Heavy rainfall and southwesterly flow after the leaving of typhoon Mindulle (2004) from Taiwan. *J. Meteor. Soc. Japan,* **86,** 17–41.

Corbosiero, K. L., J. Molinari, A. R. Aiyyer, and M. L. Black, 2006: The structure and evolution of Hurricane Elena (1985). Part II: Convective asymmetries and evidence for vortex Rossby waves. *Mon. Wea. Rev.,* **134,** 3073–3091.

Dong, J., and M. Xue, 2012: Assimilation of radial velocity and reflectivity data from coastal WSR-88D radars using ensemble Kalman filter for the analysis and forecast of landfalling hurricane Ike (2008). *Quart. J. Roy. Meteor. Soc.,* doi:10.1002/qj.1970, in press.

Du, N., M. Xue, K. Zhao, and J. Min, 2012: Impact of assimilating airborne Doppler radar velocity data using the ARPS 3DVAR on the analysis and prediction of hurricane Ike (2008). *J. Geophys. Res.,* **117,** D18113, doi:10.1029/2012JD017687.

Dvorak, V. F., 1984: Tropical cyclone intensity analysis using satellite data. NOAA Tech. Rep. NESDIS-11, 47 pp.

Fang, X., Y. H. Kuo, and A. Wang, 2011: The impact of Taiwan topography on the predictability of Typhoon Morakot's record breaking rainfall: A high-resolution ensemble simulation. *Wea. Forecasting,* **26,** 613–633.

Gander, W., G. H. Golub, and R. Strebel, 1994: Least-squares fitting of circles and ellipses. *BIT Numer. Math.,* **34,** 557–578.

Ge, X., T. Li, S. Zhang, and M. Peng, 2010: What causes the extremely heavy rainfall in Taiwan during typhoon Morakot (2009)? *Atmos. Sci. Lett.,* **11,** 46–50.

Hendricks, E. A., J. R. Moskaitis, Y. Jin, R. M. Hodur, J. D. Doyle, and M. S. Peng, 2011: Prediction and diagnosis of typhoon Morakot (2009) using Naval Research Laboratory's mesoscale tropical cyclone model. *Terr. Atmos. Oceanic Sci.,* **22,** 579–594.

Huang, C.-Y., C.-S. Wong, and T.-C. Yeh, 2011: Extreme rainfall mechanisms exhibited by typhoon Moralot (2009). *Terr. Atmos. Oceanic Sci.,* **22,** 613–632.

Jan, C.-D., F.-H. Kuo, and M.-H. Lee, 2007: A case study on debris-flow warning and evacuation during Typhoon Haitang. *Proc. Second Int. Conf. on Urban Disaster Reduction,* Taipei, Taiwan, National Science and Technology Center for Disaster Reduction, 3-3.6.

Kuo, H.-C., R. T. Williams, and J.-H. Chen, 1999: A possible mechanism for the eye rotation of typhoon Herb. *J. Atmos. Sci.,* **56,** 1659–1673.

Lee, C.-S., Y.-C. Liu, and F.-C. Chien, 2008: The secondary low and heavy rainfall associated with typhoon Mindulle (2004). *Mon. Wea. Rev.,* **136,** 1260–1283.

Li, Y., X. Wang, and M. Xue, 2012: Assimilation of radar radial velocity data with the WRF ensemble–3DVAR hybrid system for the prediction of Hurricane Ike (2008). *Mon. Wea. Rev.,* **140,** 3507–3524.

Liang, J., L. Wu, X. Ge, and C.-C. Wu, 2011: Monsoonal influence on typhoon Morakot (2009). Part II: Numerical study. *J. Atmos. Sci.,* **68,** 2222–2235.

Lin, C. Y., H. M. Hsu, Y. F. Sheng, C. H. Kuo, and Y. A. Liou, 2010: Mesoscale processes for super heavy rainfall of Typhoon Morakot (2009) over Southern Taiwan. *Atmos. Chem. Phys. Discuss.,* **10,** 13 495–13 517.

Lin, Y.-L., T.-A. Chiao, T.-A. Wang, M. L. Kaplan, and R. P. Weglarz, 2001: Some common ingredients of heavy orographic rainfall. *Wea. Forecasting,* **16,** 633–660.

——, D. B. Ensley, and C.-Y. Chiao, 2002: Orographic influences on rainfall and track deflection associated with the passage of a tropical cyclone. *Mon. Wea. Rev.,* **130,** 2929–2950.

——, S.-Y. Chen, and C. M. Hill, 2005: Control parameters for the influence of a mesoscale mountain range on cyclone track continuity and deflection. *J. Atmos. Sci.,* **62,** 1849–1866.

Lonfat, M., F. D. Marks Jr., and S. S. Chen, 2004: Precipitation distribution in tropical cyclones using the Tropical Rainfall Measuring Mission (TRMM) microwave imager: A global perspective. *Mon. Wea. Rev.,* **132,** 1645–1660.

MacDonald, N. J., 1968: The evidence for the existence of Rossby-like waves in the hurricane vortex. *Tellus,* **20,** 138–150.

Marks, F. D., 1985: Evolution of the structure of precipitation in Hurricane Allen (1980). *Mon. Wea. Rev.,* **113,** 909–930.

Möller, J. D., and M. T. Montgomery, 2000: Tropical cyclone evolution via potential vorticity anomalies in a three-dimensional balance model. *J. Atmos. Sci.,* **57,** 3366–3387.

Montgomery, M. T., and R. J. Kallenbach, 1997: A theory for vortex Rossby waves and its application to spiral bands and intensity changes in hurricanes. *Quart. J. Roy. Meteor. Soc.,* **123,** 435–465.

Nguyen, H. V., and Y.-L. Chen, 2011: High-resolution initialization and simulations of Typhoon Morakot (2009). *Mon. Wea. Rev.,* **139,** 1463–1491.

Reasor, P. D., M. T. Montgomery, F. D. Marks, and J. F. Gamache, 2000: Low-wavenumber structure and evolution of the hurricane inner core observed by airborne dual-Doppler radar. *Mon. Wea. Rev.,* **128,** 1653–1680.

Schaefer, J. T., 1990: The critical success index as an indicator of warning skill. *Wea. Forecasting,* **5,** 570–575.

Smith, R. B., and I. Barstad, 2004: A linear theory of orographic precipitation. *J. Atmos. Sci.,* **61,** 1377–1391.

Tuleya, R. E., M. DeMaria, and R. J. Kuligowski, 2007: Evaluation of GFDL and simple statistical model rainfall forecasts for U. S. landfalling tropical storms. *Wea. Forecasting,* **22,** 56–70.

Wang, Y., 2002a: Vortex Rossby waves in a numerically simulated tropical cyclone. Part II: The role in tropical cyclone structure and intensity changes. *J. Atmos. Sci.,* **59,** 1239–1262.

——, 2002b: Vortex Rossby waves in a numerically simulated tropical cyclone. Part I: Overall structure, potential vorticity, and kinetic energy budgets. *J. Atmos. Sci.,* **59,** 1213–1238.

——, 2008: Rapid filamentation zone in a numerically simulated tropical cyclone. *J. Atmos. Sci.,* **65,** 1158–1181.

Whitaker, J. S., T. M. Hamill, X. Wei, Y. Song, and Z. Toth, 2008: Ensemble data assimilation with the NCEP Global Forecast System. *Mon. Wea. Rev.,* **136,** 463–482.

Wilks, D. S., 2006: *Statistical Methods in the Atmospheric Sciences.* 2nd ed. Academic Press, 648, pp.

Wu, C.-C., and M.-J. Yang, 2011: Preface to the special issue on ''Typhoon Morakot (2009): Observation, modeling, and forecasting.'' *Terr. Atmos. Oceanic Sci.,* **22,** doi:10.3319/TAO.2011.10.01.01(TM).

——, T.-H. Yen, Y.-H. Kuo, and W. Wang, 2002: Rainfall simulation associated with typhoon Herb (1996) near Taiwan. Part I: The topographic effect. *Wea. Forecasting,* **17,** 1001–1015.

——, H.-J. Cheng, Y. Wang, and K.-H. Chou, 2009a: A numerical investigation of the eyewall evolution in a landfalling typhoon. *Mon. Wea. Rev.,* **137,** 21–40.

——, K. K. W. Cheung, and Y.-Y. Lo, 2009b: Numerical study of the rainfall event due to the interaction of typhoon Babs (1998) and the northeasterly monsoon. *Mon. Wea. Rev.,* **137,** 2049–2064.

Wu, L., J. Liang, and C.-C. Wu, 2011: Monsoonal influence on typhoon Morakot (2009). Part I: Observational analysis. *J. Atmos. Sci.,* **68,** 2208–2221.

Xue, M., K. K. Droegemeier, V. Wong, A. Shapiro, and K. Brewster, cited 1995: ARPS version 4.0 user's guide. Center for Analysis and Prediction of Storms, 380 pp. [Available online at http://www.caps.ou.edu/ARPS.]

——, ——, and ——, 2000: The Advanced Regional Prediction System (ARPS)—A multiscale nonhydrostatic atmospheric simulation and prediction tool. Part I: Model dynamics and verification. *Meteor. Atmos. Phys.,* **75,** 161–193.

——, and Coauthors, 2001: The Advanced Regional Prediction System (ARPS)—A multiscale nonhydrostatic atmospheric simulation and prediction tool. Part II: Model physics and applications. *Meteor. Atmos. Phys.,* **76,** 143–165.

——, D.-H. Wang, J.-D. Gao, K. Brewster, and K. K. Droegemeier, 2003: The Advanced Regional Prediction System (ARPS), storm-scale numerical weather prediction and data assimilation. *Meteor. Atmos. Phys.,* **82,** 139–170.

Yang, M.-J., D.-L. Zhang, and H.-L. Huang, 2008: A modeling study of typhoon Nari (2001) at landfall. Part I: Topographic effects. *J. Atmos. Sci.,* **65,** 3095–3115.

Zhang, F., Y. Weng, Y.-H. Kuo, J. S. Whitaker, and B. Xie, 2010: Predicting Typhoon Morakot's catastrophic rainfall with a convection-permitting mesoscale ensemble system. *Wea. Forecasting,* **25,** 1816–1825.

Zhang, Q., Q. Liu, and L. Wu, 2009: Tropical cyclone damages in China 1983–2006. *Bull. Amer. Meteor. Soc.,* **90,** 489–495.

Zhao, K., and M. Xue, 2009: Assimilation of coastal Doppler radar data with the ARPS 3DVAR and cloud analysis for the prediction of Hurricane Ike (2008). *Geophys. Res. Lett.,* **36,** L12803, doi:10.1029/2009GL038658.

——, X. Li, M. Xue, B. J.-D. Jou, and W.-C. Lee, 2012: Short-term forecasting through intermittent assimilation of data from Taiwan and Mainland China coastal radars for typhoon Meranti (2010) at landfall. *J. Geophys. Res.,* **117,** D06108, doi:10.1029/2011JD017109.